Electronic Supplementary Information (ESI) for

A sumanene-containing magnetic nanoadsorbent for the removal of caesium salts from aqueous solutions

Artur Kasprzak,*[a] Magdalena Matczuk[b], and Hidehiro Sakurai[c,d]

[a]   Chair of Organic Chemistry, Faculty of Chemistry, Warsaw University of Technology, 00-664 Warsaw, Poland

* corresponding author e-mail: artur.kasprzak@pw.edu.pl (A.K.)

[b]   Chair of Analytical Chemistry, Faculty of Chemistry, Warsaw University of Technology, 00-664 Warsaw, Poland

[c]   Division of Applied Chemistry, Graduate School of Engineering, Osaka University, Suita 565-0871, Osaka, Japan

[d]   Innovative Catalysis Science Division, Institute for Open and Transdisciplinary Research Initiatives (ICSOTRI), Osaka University, Suita 565-0871 Osaka, Japan

Table of Contents

S1. Experimental section

S1.1. Materials and methods

Chemical reagents and solvents for the synthesis were commercially purchased and purified according to the standard methods, if necessary. Cobalt nanomagnets[1] **6** were purchased from Merck, product number 697745. Anhydrous $MgSO_4$ was used as a drying agent. Volatiles were distilled off under reduced pressure on a rotating evaporator. Thin layer chromatography (TLC) and preparative thin layer chromatography (PTLC) were performed using Merck Silica gel 60 F254 plates. Sonication was performed with a Bandelin Sonorex RK 100 H ultrasonic probe with a temperature control (ultrasonic peak output/HF power: 320W/80W; 35 kHz). Shaking was performed with a Multi Vortex-Genie Digital laboratory shaker.

NMR. The NMR experiments were carried out using a Varian VNMRS 500 MHz spectrometer (^{1}H NMR at 500 MHz, ^{13}C{^{1}H} NMR at 125 MHz) equipped with a multinuclear z-gradient inverse probe head. The spectra were recorded at 25 °C and standard 5 mm NMR tubes were used. ^{1}H chemical shifts (δ) were reported in parts per million (ppm) relative to the solvent signal, *i.e.*, DMSO-d_6: δ_H (residual DMSO) 2.50 ppm, δ_C (residual DMSO) 39.5 ppm, CDCl$_3$: δ_H (residual CHCl$_3$) 7.26 ppm. NMR spectra were sanalysed with the MestReNova v12.0 software (Mestrelab Research S.L).

HRMS. ESI-HRMS (TOF) measurements were performed with a Q-Exactive ThermoScientific spectrometer.

UV-vis. UV-vis spectra were recorded with a WVR UV-1600PC spectrometer, with the spectral resolution of 2 cm^{-1}.

Emission spectroscopy. Emission spectra were recorded with a HITACHI F-7100 FL spectrometer, parameters: scan speed: 1200 nm/mim, delay: 0.0 s, EX slit: 5.0 nm, EM slit: 5.0 nm, PMT voltage: 400 V.

FT-IR. Fourier-transform infrared (FT-IR) spectra were recorded in a transmission mode with a Thermo Scientific Nicolet iS5 spectrometer with a spectral resolution of 4 cm^{-1}. The samples were mixed with spectrally pure potassium bromide and pressed in the form of pellets.

PXRD. Powder X-ray diffraction (PXRD) measurements were carried out at room temperature on a Bruker D8 Advance diffractometer equipped with a position sensitive LYNXEYE detector and a Cu sealed tube (λ = 1.5418 Å). Diffraction patterns were recorded in Bragg-Brentano horizontal geometry from 5° to 30° (2θ) with steps of 0.03° and 576 s/step. The diffractometer incident beam path was equipped with a 2.5° Soller slit, and a 1.14° fixed divergence slit, while the diffracted beam path was equipped with a programmable antiscatter slit (fixed at 2.20°), a Ni β-filter, and a 2.5° Soller slit.

Raman spectroscopy. Raman spectroscopy analyses were warried out with a Bruker IFS66 instrument equipped with a FRA 106 FTRaman module and a Nd:YAG laser (1064 nm) as a laser source.

XPS. X-ray photoelectron spectroscopic (XPS) measurements were performed using a PHI 5000 VersaProbe (ULVAC-PHI) spectrometer with monochromatic Al Kα radiation (hν = 1486.6 eV) from an X-ray source operating at 100 µm spot size, 25 W

and 15 kV. The high-resolution (HR) XPS spectra were collected with the hemispherical analyser at the pass energy of 23.5 and the energy step size of 0.1 eV. The X-ray beam was incident at the sample surface at the angle of 45° with respect to the surface normal, and the analyser axis was located at 45° with respect to the surface.

TGA. Thermogravimetric analysis (TGA) was performed with a Mettler Toledo TGA instrument under nitrogen atmosphere, with a heating rate of 10 °C·min^{-1}.

Elemental analysis. Elemental analyses were performed using CHNS Elementar Vario EL III apparatus. Each elemental composition was reported as an average of two analyses.

TEM and SEM. Transmission electron microscopy (TEM) results were obtained using a Talos F200X HRTEM microscope equipped. The SEM analyses were performed at low kV electron beam energy (3 kV, 30 pA current). Before the examination, each sample was covered with a 1-2 nm thin film of Au-Pd alloy to avoid electrical charging of the sample surface. The layers of the alloy were sputtered using a Polaron SC7620 Mini Sputter Coater.

Zeta potential and dynamic light scattering (DLS) measurements. Zeta potential and DLS measurements were performed with a Zetasizer Nano ZS Malvern Panalytical (UK) instrument. The surface zeta measurements were carried out at 25°C with the dispersions in distilled water. The measured surface zeta potential (in mV) was taken as the average from three independent measurements.

ICP-MS/MS. Aliquots of the solutions after adsorption tests were diluted adequately (from 10- to 1000-times) in 2% (v/v) nitric acid (HNO$_3$, 69%, Sigma-Aldrich, trace metal basis), and yttrium as internal standard was added (5 µg/L final Y concentration, Merck). In comparison, the nanoadsorbent solid samples were digested. Namely, from the laboratory samples, two analytical samples were weighed into Teflon vessels (with an accuracy of 0.0001 g). 5 mL of concentrated HNO$_3$ (69%, Sigma-Aldrich, trace metal basis) and 1 mL of hydrogen peroxide (30%, Sigma-Aldrich, trace metal basis) were added to each vessel. After 5 min, vessels were closed, and samples were digested in M6 microwave-assisted digestion system (PreeKem Scientific Instruments) in the temperature program: heating to 130 °C, 10 min stabilisation, heating to 180 °C, and 15 min stabilisation. After cooling down, the liquids from the vessels were quantitatively transferred into volumetric 100 mL flasks (class A), filled up with ultrapure water R≥18.2 MΩ cm^{-1} (Millipore Milli-Q, Merck Millipore), and mixed. Then aliquots of samples were diluted analogically as described above. The concentrations of caesium and/or potassium and/or sodium in samples were determined using an inductively coupled plasma tandem mass spectrometer working as an element-specific detector (each sample was measured in 20 repetitions). The Agilent 8900 ICP Triple Quadrupole Mass Spectrometer was equipped with a 2.5 mm quartz torch and the Pt-cones in the interface. The position of the torch and the nebuliser gas flow were adjusted daily, with emphasis paid to the increase in the signal-to-noise ratio using a 1 µg/L solution of Co, Y, Ce and Tl in 2% (v/v) HNO$_3$ and 2% (v/v) HNO$_3$, respectively. The RF power was 1430 W, the nebuliser gas flow was 1.05 L/min, and the reaction gas flow (hydrogen in ICP-MS/MS) was 5.5 mL/min.

The total concentrations of selected metals in measured samples were calculated automatically as a result of monitoring the singly-positively charged ions with the specified mass/charge ratios: 133 (^{133}Cs), 39 (^{39}K), 23 (^{23}Na) registered in the

on-mass mode after the production in the collision-reaction cell, and normalisation (^{89}Y) after daily external calibration against 15-point calibration curve (0–800 µg/L, $R^2 >$ 0.9995). The example of the calibration curve obtained for caesium, barium and nickel determination by the internal standard method (the ratio of analyte signal on the internal standard signal on the OY axis) is presented in **Fig. S1**-**Fig. S3**. The obtained limits of detection of analytes were: Cs 0.0032, K 0.7926, Na 2.4576, Ba 0.0430, Ni 0.420 µg/L.

The elements' concentrations in liquid samples, produced after adsorption tests, were calculated by multiplying the generated in the software values by the samples' dilution factor. In comparison, the contents of elements in solid adsorbents were obtained from more specified mathematical operations. Namely, the concentration generated in the software was multiplied by the dilution factor, and then the mass of the element in a 100 mL volumetric flask was calculated. The analyte content (in mg) per 1 g of adsorbent was obtained knowing the exact mass of the weighted material, which was undergoing digestion, and then put into the mentioned above flask.
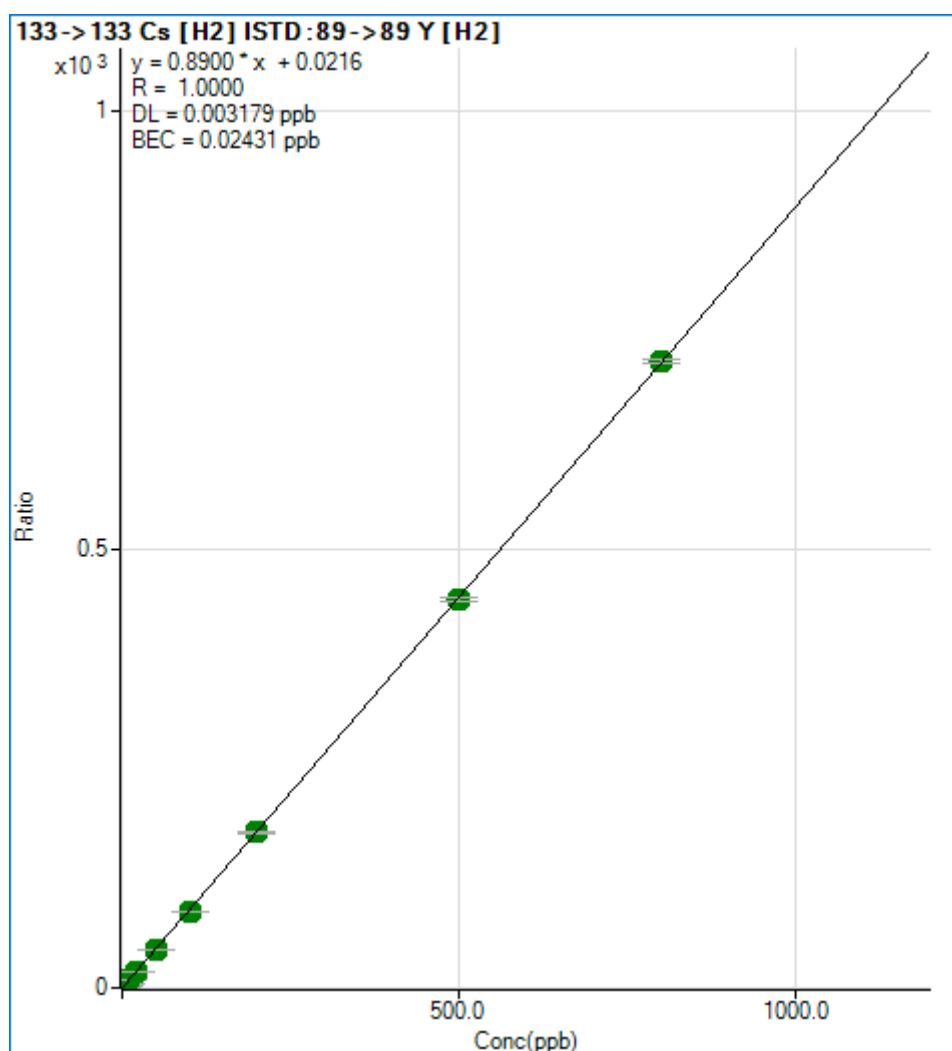

Fig. S1 ICP-MS/MS calibration curve generated for the quantitative analysis of caesium by the internal standard method.
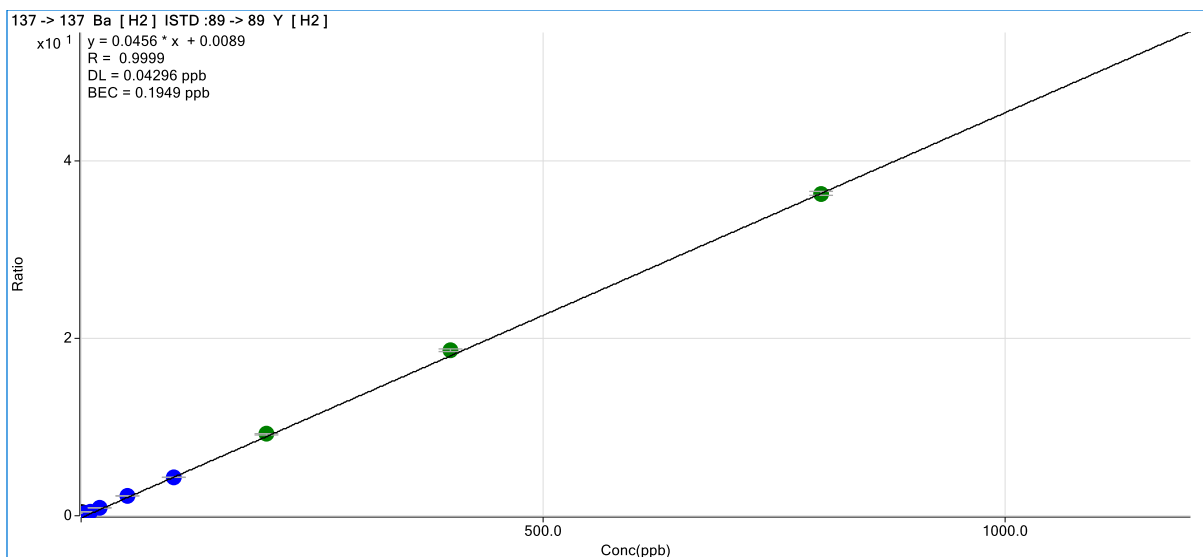
Fig. S2 ICP-MS/MS calibration curve generated for the quantitative analysis of barium by the internal standard method.
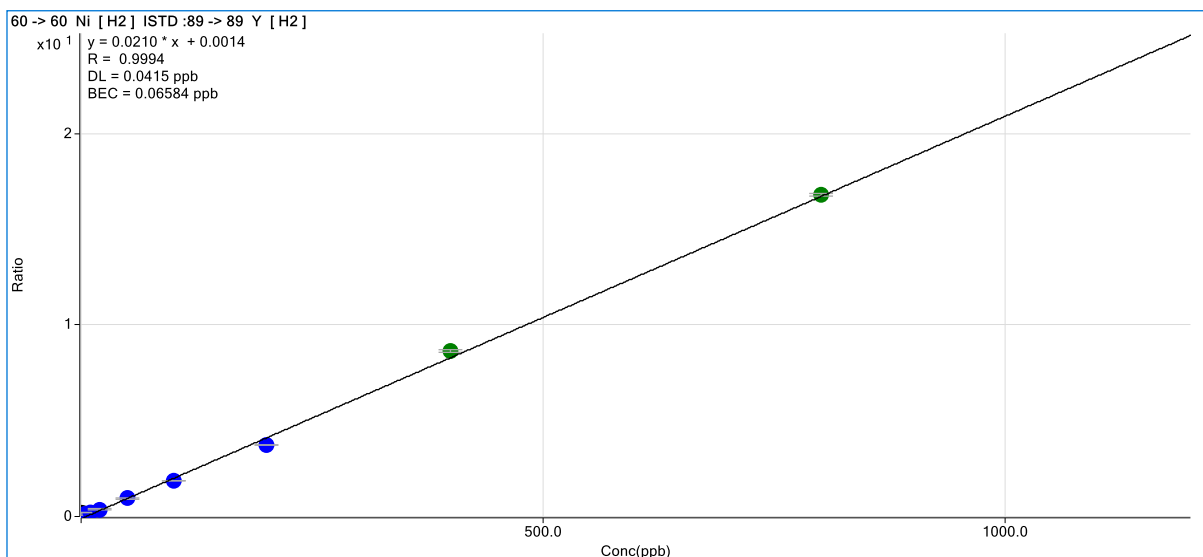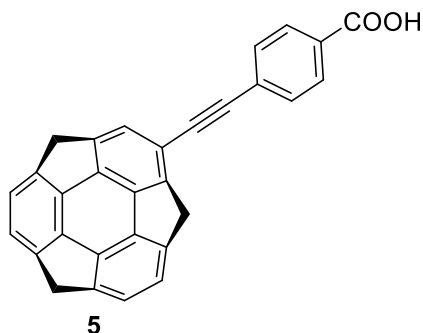

Fig. S3 ICP-MS/MS calibration curve generated for the quantitative analysis of nickel by the internal standard method.

S1.2. Synthesis of sumanene derivative 5

Sumanene (**1**)[1] and 2-iodosumanene (**3**)[2] were synthesised according to the literature procedures.

Synthesis of compound 5 (4-((4,7-dihydro-1H-tricyclopenta[def,jkl,pqr]triphenylen-2-yl)ethynyl)benzoic acid)


5

A solution of 2-iodosumanene (**3**; 150 mg, 0.39 mmol, 1.00 eq), bis(triphenylphosphine)palladium(II) dichloride (Pd(PPh$_3$)Cl$_2$; 27.5 mg, 0.039 mmol, 0.10 eq) and copper(I) iodide (CuI; 3.8 mg, 0.0195 mmol, 0.05 eq) in triethylamine (TEA; 15 mL) and tetrahydrofuran (THF; 15 mL) was stirred at 50°C for 15 minutes under argon atmosphere. A solution of 4-ethynylbenzoic acid (**4**; 76.1 mg, 0.585 mmol, 1.50 eq) in TEA (15 mL) and THF (35 mL) was added, and the reaction mixture was stirred at 50°C for 24 hours under argon atmosphere. Distilled water (20 mL) was added. The reaction mixture was extracted with dichloromethane (3 x 70 mL), washed several times with 2 M HCl$_{aq}$ (10 mL per each washing), water (2 x 20 mL), brine (2 x 20 mL), dried over MgSO$_4$. After filtration, volatiles were distilled off using a rotary evaporator. The crude reaction mixture was purified using a column chromatography (6% CH$_3$OH/CH$_2$Cl$_2$) to provide 114.7 mg (72%) of 4-((4,7-dihydro-1H-tricyclopenta[def,jkl,pqr]triphenylen-2-yl)ethynyl)benzoic acid (**5**) as brownish-white solid.

^{1}H NMR (500 MHz, DMSO-d_6, ppm) δ_H 12.48 (bs, 1H), 7.98-7.96 (m, 2H), 7.67-7.66 (m, 2H), 7.36 (s, 1H), 7.25-7.21 (m, 4H), 4.84 (d, $^2J_{H-H}$ = 20.4 Hz, 1H), 4.74 (d, $^2J_{H-H}$ = 19.6 Hz, 1H), 4.72 (d, $^2J_{H-H}$ = 20.4 Hz, 1H), 3.68 (d, $^2J_{H-H}$ = 20.4 Hz, 1H), 3.60 (d, $^2J_{H-H}$ = 19.7 Hz, 1H), 3.54 (d, $^2J_{H-H}$ = 20.2 Hz, 1H); ^{13}C{^{1}H} NMR (125 MHz, DMSO-d_6, ppm) δ_C 166.9, 151.5, 149.6, 149.3, 149.1, 148.6, 148.4, 148.3, 148.2, 147.5, 147.4, 147.3, 131.5, 129.6, 126.9, 124.6, 124.5, 124.0x2, 116.7, 91.5, 90.2, 41.5, 41.4, 41.3; HRMS (ESI) m/z [M+H]$^+$ calcd. For C$_{30}$H$_{17}$O$_2$ 409.1223, found 409.1224; UV-vis, λ_{max} (DMSO; 2·10^{-5} M) 292, 342 nm; Emission spectrum, λ_{max} (DMSO; 2·10^{-5} M, λ_{ex} = 340 nm) 402 nm; R$_F$ (6% CH$_3$OH/CH$_2$Cl$_2$) = 0.30.

S1.3. Synthesis of the magnetic nanoadsorbent 11

*Synthesis of material 8*

8
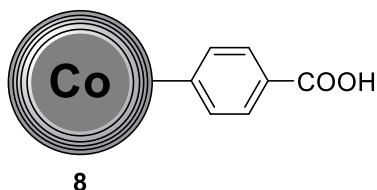
To a solution of 4-aminobenzoic acid (**7**; 1.4399 g, 10.5 mmol) in distilled water (140 mL) and concentrated HCl_{aq} (4.25 mL), a solution of sodium nitrite ($NaNO_2$; 1.0971 g, 15.9 mmol) in distilled water (85 mL) was slowly added in the temperature range of 0-5°C. This solution was added in one portion to the dispersion of cobalt nanomagnets (**6**; 2.0000 g) in distilled water (13.5 mL). The reaction mixture was sonicated for 30 minutes at 25°C. The material was then separated from the reaction mixture by using a permanent neodymium magnet, and the supernatant was discarded. The material was then toughly washed several times with water, ethanol, ethyl acetate and dichloromethane (DCM). After drying for 24 hours at 45°C, 2.1501 g of target material **8** was obtained.

Synthesis of material 10

10
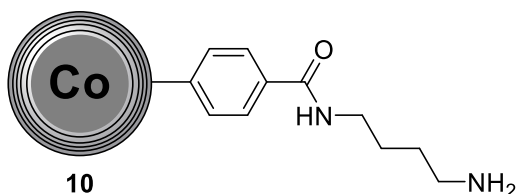
A solution of material **8** (1.5000 g) in DCM (50 mL) was sonicated for 10 minutes at 25°C. Solid *N*-hydroxysuccinimide (NHS; 115.09 mg, 1 mmol) and *N*-(3-dimethylaminopropyl)-*N′*-ethylcarbodiimide hydrochloride (EDCl; 191.7 mg, 1 mmol) were added, and the mixture was sonicated for 30 minutes at 25°C. *N*-Boc-1,4-butanediamine (**9**; 192.0 μL; 188.3 mg, 1 mmol) was added, and the reaction mixture was sonicated for 4 hours at 25°C. The material was then separated from the reaction mixture by using a permanent neodymium magnet, and the supernatant was discarded. The material was then toughly washed several times with ethanol, and DCM. The wet material was suspended in DCM (50 mL) and sonicated for 5 minutes at 25°C. Trifluoroacetic acid (TFA; 15 mL) was slowly added, and the reaction mixture was sonicated for 30 minutes at 25°C. The material was then separated from the reaction mixture by using a permanent neodymium magnet, and the supernatant was discarded. The material was then toughly washed several times with DCM. After drying for 24 hours at 45°C, 1.6821 g of target material **10** was obtained.

Synthesis of the magnetic nanoadsorbent (material *11*)
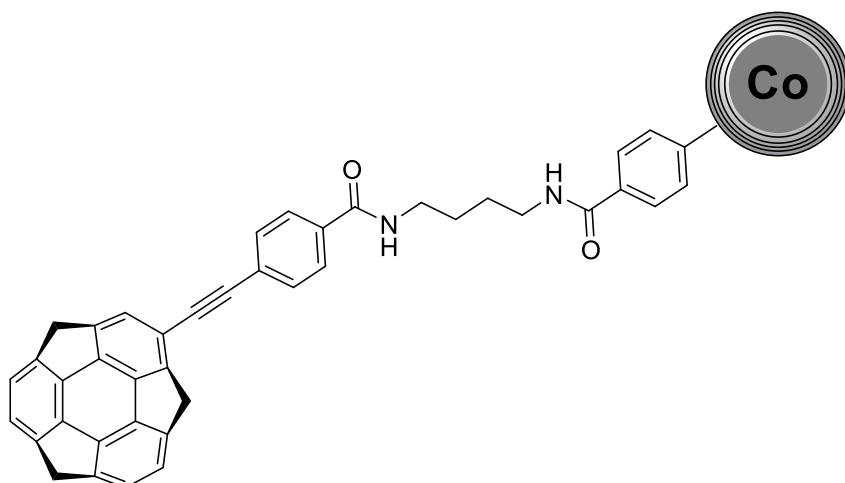
11

To a solution of compound **5** (110 mg, 0.27 mmol) in *N*,*N*-dimethylformamide (DMF; 50 mL), solid NHS (62.2 mg, 0.54 mmol) and EDCI (103.68 mg, 0.54 mmol) were added, and the mixture was stirred for 1 hour at room temperature. This solution was added into the dispersion of material **10** 1.0000 g) in DMF (10 mL). The reaction mixture was sonicated for 4 hours at 25°C. The material was then separated from the reaction mixture by using a permanent neodymium magnet, and the supernatant was discarded. The material was then toughly washed several times with DMF, ethanol, and DCM. After drying for 24 hours at 45°C, 1.1054 g of target material **11** was obtained.

S2. Characterisation data

S2.1. Characterisation data for sumanene derivative 5
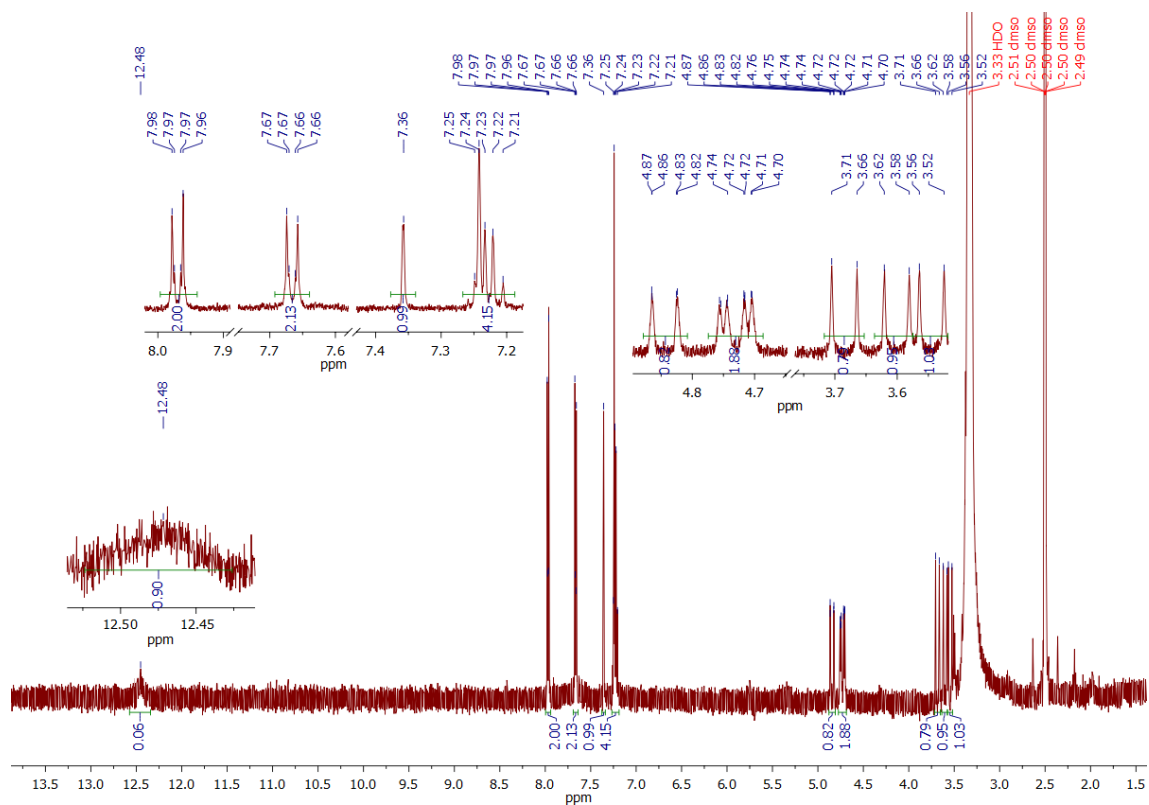
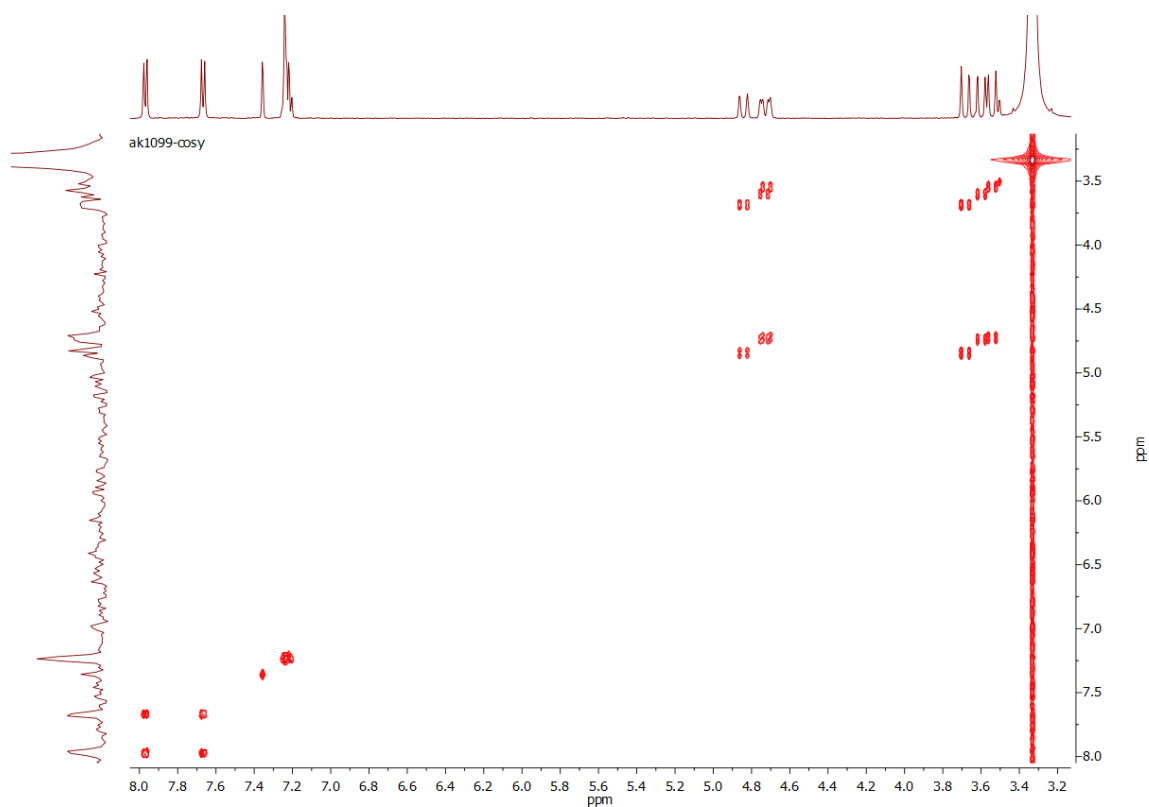**Fig. S4** ^{1}H NMR (500 MHz, DMSO-d_6) spectrum of compound **5**.

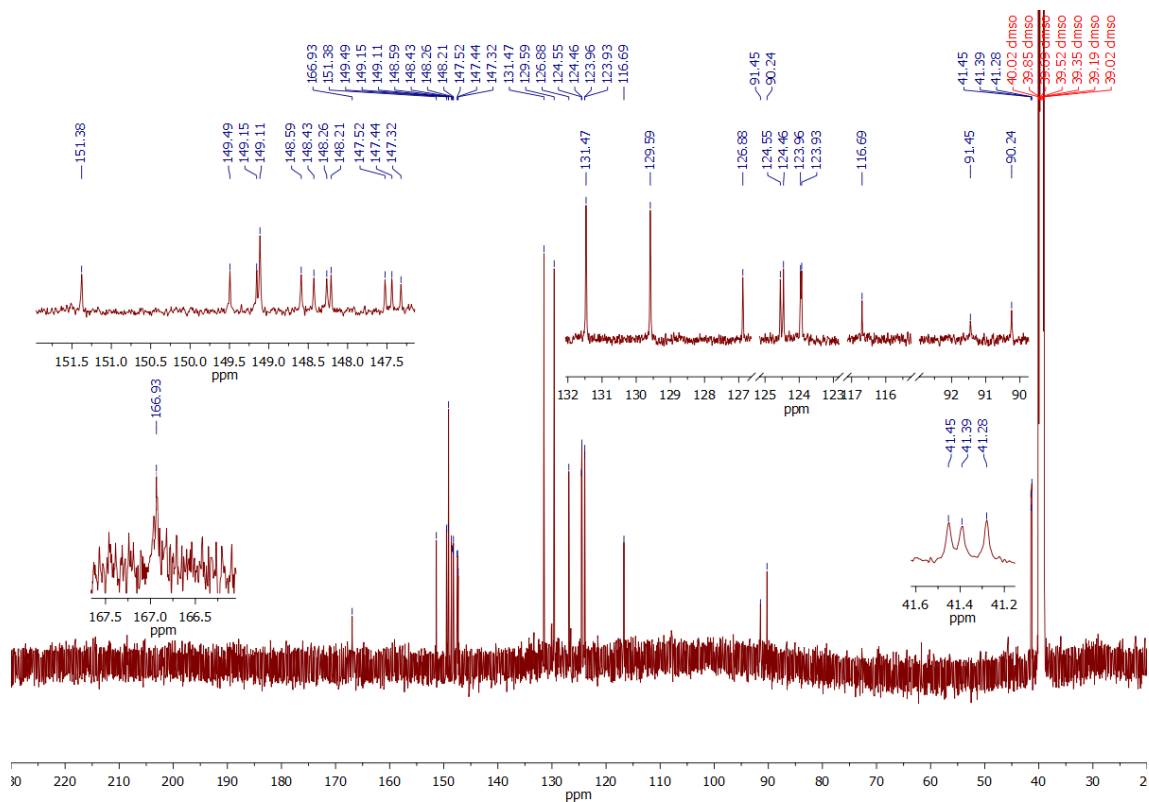**Fig. S5** ^{1}H-^{1}H COSY NMR (500 MHz, DMSO-d_6) spectrum of compound **5**.

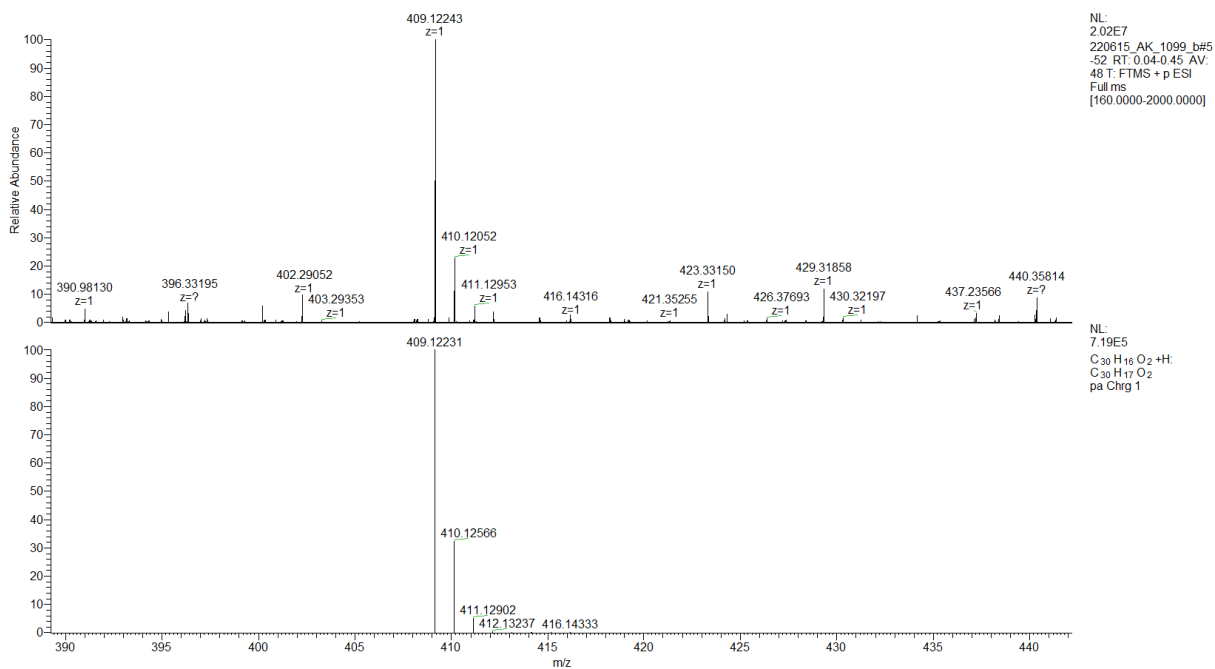**Fig. S6** $^{13}C\{1H\}$ NMR (125 MHz, DMSO-d_6) spectrum of compound **5**.

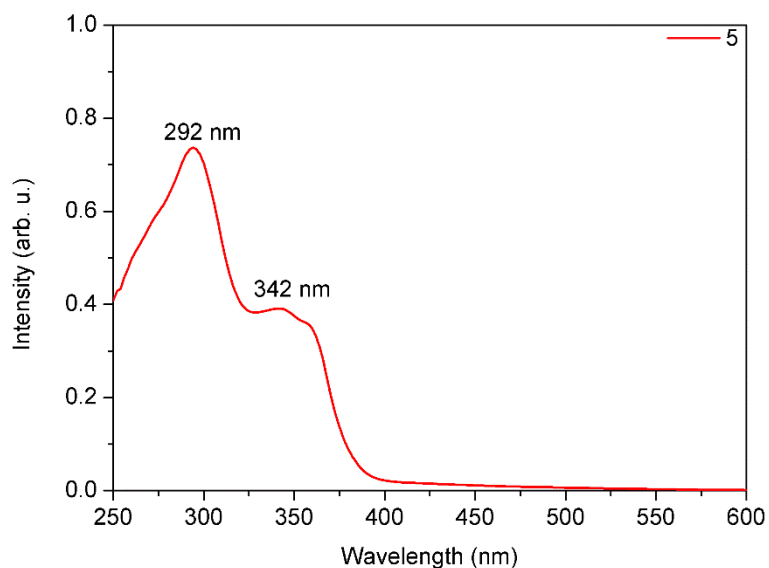**Fig. S7** HRMS spectrum of compound **5**.

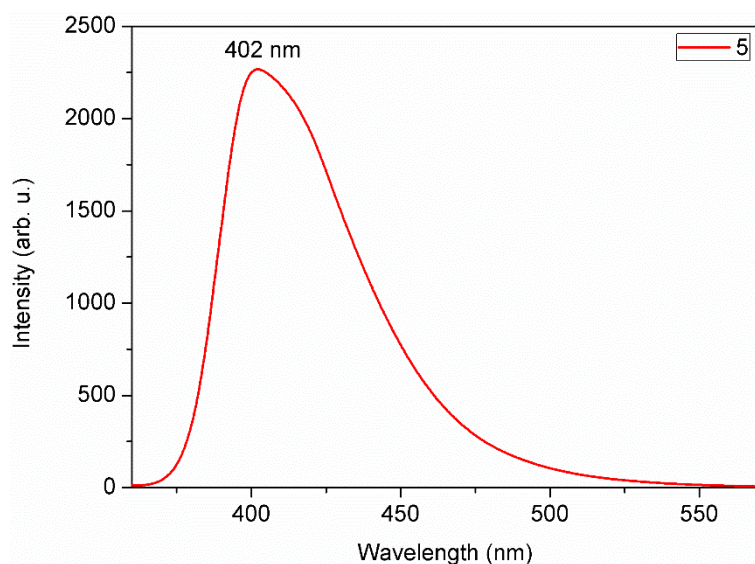**Fig. S8** UV-vis spectrum ($2 \cdot 10^{-5}$ M; DMSO) of compound **5**.

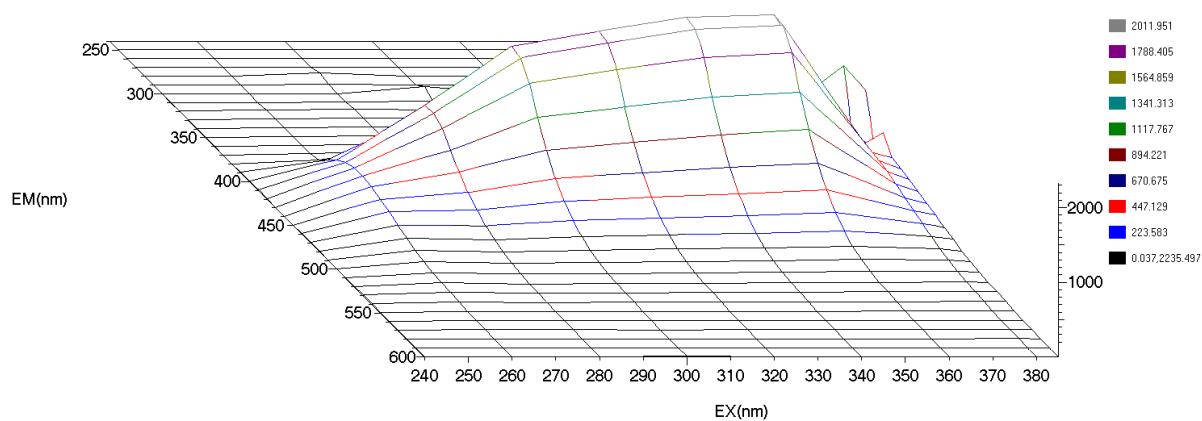**Fig. S9** Emission spectrum ($2 \cdot 10^{-5}$ M; DMSO; λ_{ex} = 340 nm) of compound **5**.

Fig. S10 3-D Emission spectrum ($2 \cdot 10^{-5}$ M; DMSO) of compound **5**. Compound **5** shows the highest emission intensity at λ_{ex} = 360 nm (λ_{em} = *ca*. 400 nm).

S2.2. Characterisation data for the magnetic nanoadsorbent 11

Fourier-transform infrared (FT-IR) spectra (measured in a transmittance mode in a form of KBR pellets) of materials **6**, **8**, **10** and **11** are presented in **Fig. S11**. The spectrum of pure cobalt nanomagnets **6** do not feature any significant absorption bands.[3,4] On the contrary, several medium- or low-intensity absorption bands can be found in the spectra of functionalised materials **8**, **10** and **11**, which is the result of the modification of carbon layer of nanoparticles.[3–5] In the case of material **8** (cobalt nanomagnets sfunctionalised to carboxylic functionalities), the most intense absorption band located at *ca*. 1700 cm^{-1} is ascribed to the C=O vibrations within carboxylic groups. Material **10**, comprising the amide bonds, feature the most significant absorption band at *ca*. 1635 cm^{-1}. This band is ascribed to the vibrations within amide bond (amide-I band). Notably, this peak is shifted in comparison to the parent material **8** (1700 cm^{-1} *vs* 1635 cm^{-1}), which is characteristic for the modification of carboxylic groups to the amide moieties. FT-IR spectrum of material **10** also features adsorption bands located at *ca*. 1380 cm^{-1} and in the range of *ca*. 1280-1050 cm^{-1}, which are ascribed to the N-H and C-N vibrations within amino and amide groups, and C-H vibrations within methylene moieties, respectively. The FT-IR spectrum of target material **11** features several adsorption bands similar to parent material **10**, including the absorption bands coming from the C=O vibrations within an amide group (*ca*. 1620 cm^{-1}), and absorption bands coming from the C-N and C-H (methylene groups) vibrations (*ca*. 1390 cm^{-1} and *ca*. 1245-1035 cm^{-1}). Notably, the relative intensity of the absorption band at *ca*. 1620 cm^{-1} is higher in comparison to the intensity in the parent sample **10**. It is ascribed to the higher content of amide bonds in material **11** in comparison to material **10**. Additionally, the number of low- and medium-intensity absorption bands in the area *ca*. 1480-1035 cm^{-1}) can be found in the spectrum of **11**. It is ascribed to the introduction of sumanene moieties to the surface of the material **11**.
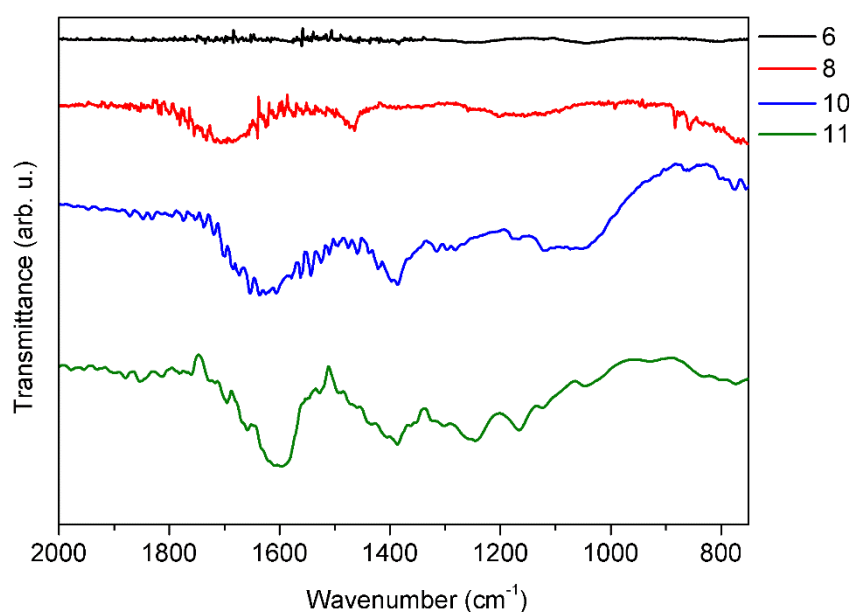

Fig. S11 FT-IR spectra of materials **6**, **8**, **10** and **11**.

The X-ray diffraction patterns of materials **6**, **8**, **10** and **11** that comprise the cobalt nanomagnets reveal the characteristic reflexes for the face centred cubic (fcc) cobalt (fcc-Co)[6], confirming the presence of cobalt in all samples (**Fig. S12**). Lowering the intensity of reflexes coming from the cobalt for the subsequent modified materials (**6**, **8**, **10** and **11**) might suggest lowering the mass content of cobalt in the samples. It is ascribed to attaching next surface moieties onto the carbon surface of cobalt nanomagnets.
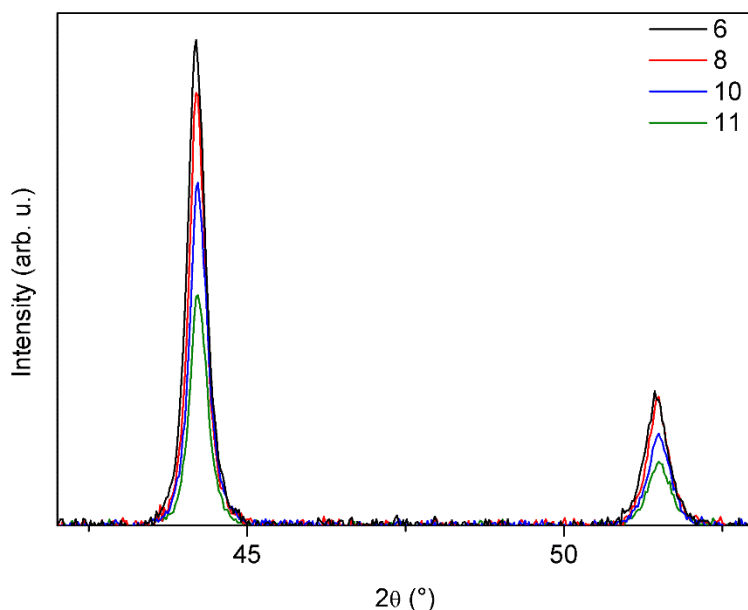

Fig. S12 The X-ray diffraction patterns of materials **6**, **8**, **10** and **11**.

Raman spectra analyses further support the surface modification of cobalt nanomagnets (**Fig. S15**). Raman spectrum of pure cobalt nanomagnets (**6**) comprise two major peaks cantered at *ca*. 1345 cm^{-1} and 1590 cm^{-1}, which are attributed to the characteristic signals for the graphene-family materials, *i.e.*, D-band and G-band, respectively. An increase in the intensity of D-band (I_D) with the respect to the in the intensity of G-band (I_G) between the samples (materials **6**, **8**, **10** and **11**) is observed. It is ascribed to the subsequent introduction of next surface moieties onto the carbon surface. Surface modification of carbon layer causes lowering its graphitisation, thus I_G of the material observed in Raman spectrum. The most significant difference in I_D band between materials **8** and **10** among all samples is ascribed to the attachment of aliphatic moieties (CH_2) at this reaction step. Slight lowering of the I_D band between material **10** and **11** might be a result of introducing aromatic moieties (*p*-phenylene and sumanene skeletons) at this reaction step.
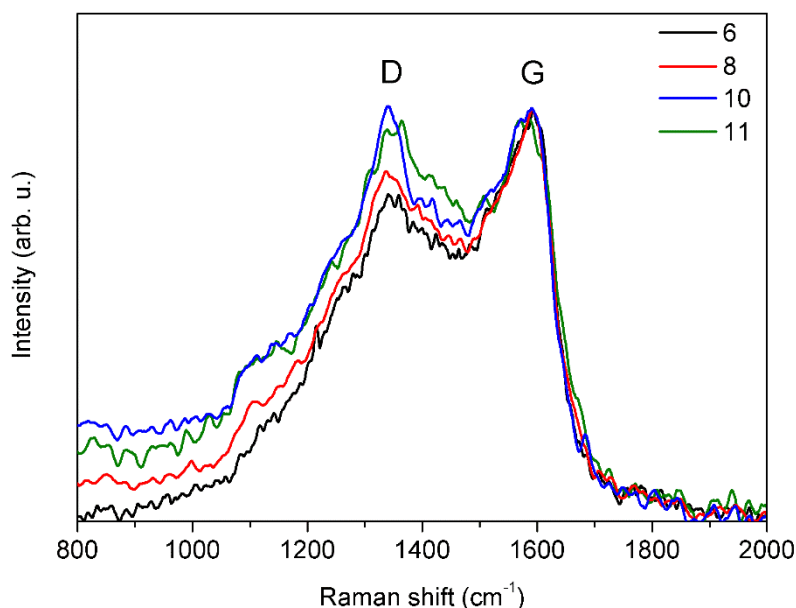
Fig. S13 Raman spectra of materials **6**, **8**, **10** and **11**. The intensity of G-band (I_G) of cobalt nanomagnets (**6**) was used as the reference to compare the relative intensities of D-band and G-band of the samples.

The X-ray photoelectron spectra (XPS) of target material **11** and cobalt nanomagnets **6** are presented in **Fig. S15**. These analyses also support the successful reaction pathway. Most importantly, the survey spectrum of material **11** (**Fig. S15a**) reveal the presence of four major components of the sample, namely carbon, nitrogen, oxygen and cobalt, what confirms the successful modification of the carbon layer of cobalt nanomagnets **6**. Further conclusions were drawn by analysing the deconvoluted C1s and N1s components. The deconvoluted C1s component of in the spectrum of material **11** (**Fig. S15b**) comprises at least three peaks, centred at 295.7 eV and 283.2-282.5 eV. The first band (295.7 eV) is characteristic for the C=O groups, what supports the presence of this motif in the material in the form of amide linkages. The latter features (283.2-282.5 eV) are ascribed to the sp2 carbons from the carbon layer and introduced moieties, and for the sp carbons from the introduced moieties. For comparison, the C1s component of native cobalt nanomagnets **6** (**Fig. S15c**) comprises only one peak, centred at 284.4 eV and corresponds to sp2 carbons of the carbon layer. Finally, the success of the designed reaction pathway is also supported by the presence of the N1s component in the spectrum of material **11** (**Fig. S15d**). It comprises mainly one peak centred at 397.9 eV, which originates from the presence of C-N bonds in the material. For comparison, the survey spectrum of cobalt nanomagnets do not comprise the N1s component (**Fig. S15e**). The inset to the Co 2p component of material **11** is presented in **Fig. S15f**, and further supports the presence of cobalt in the sample.
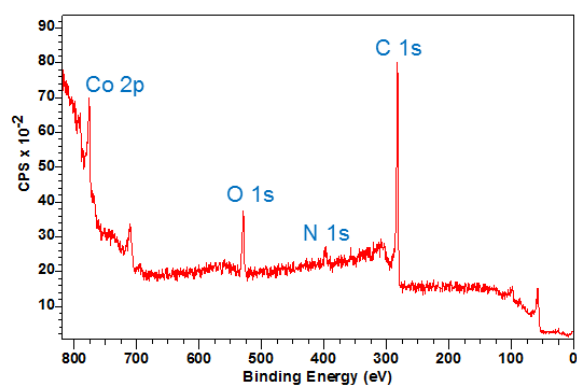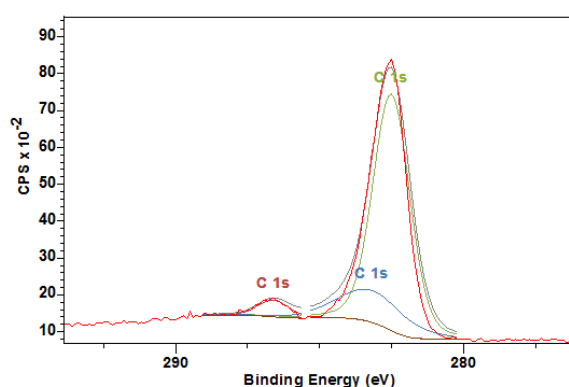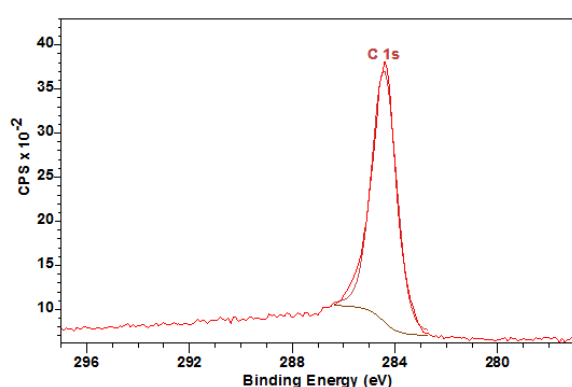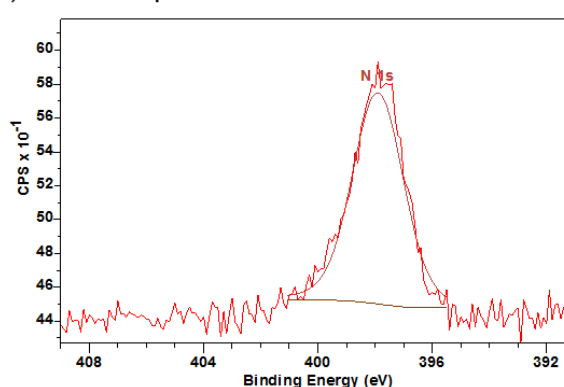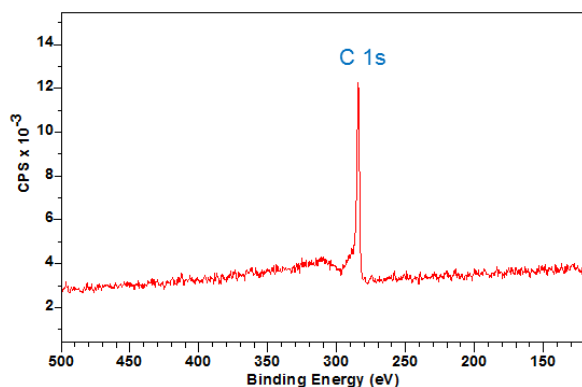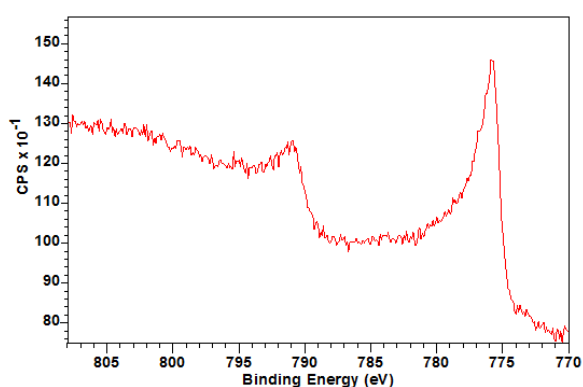
a) survey spectrum of **11**

b) C1s component of **11**

c) C1s component of **6**

d) N1s component of **11**

e) Inset of the survey spectrum of **6**

f) Co 2p component of **11**

Fig. S14 The XPS spectra of material **11**, together with the selected comparisons with the spectra of cobalt nanomagnets **6**. The insets to the given components are also shown.

The thermogravimetric analysis (TGA) provided an insight in the mass content of sumanene in the sample of material **11**. TGA curves feature the higher weight loss in the range up to 400°C for materials **8**, **10** and **11** in comparison to parent cobalt nanomagnets **6** (**Fig. S15**). The weight losses were not the same for all samples. These differences in weight loss are attributed to the introduction of subsequent moieties onto the surface of nanoparticles. The estimated content of sumanene in material **11** is *ca*. 9 wt%.
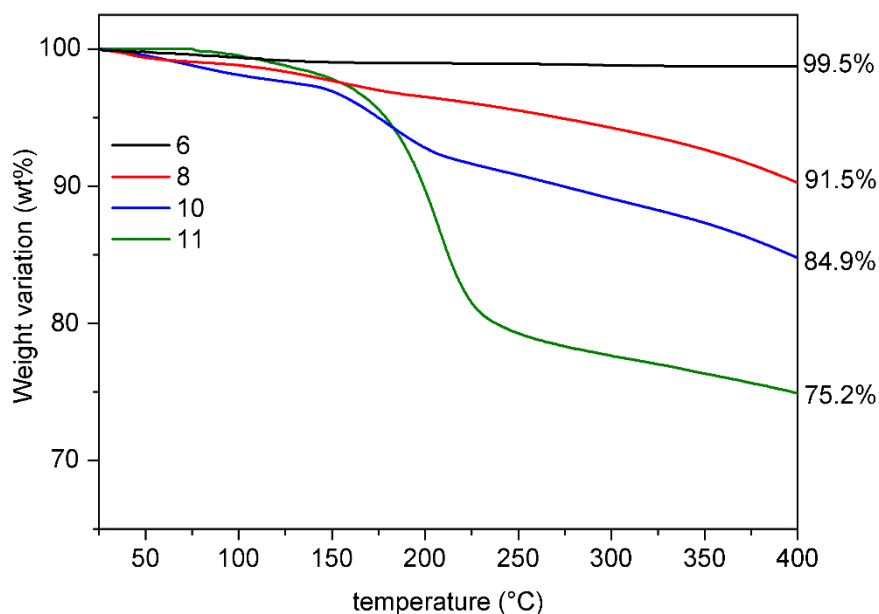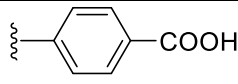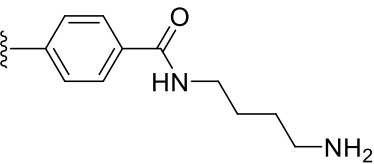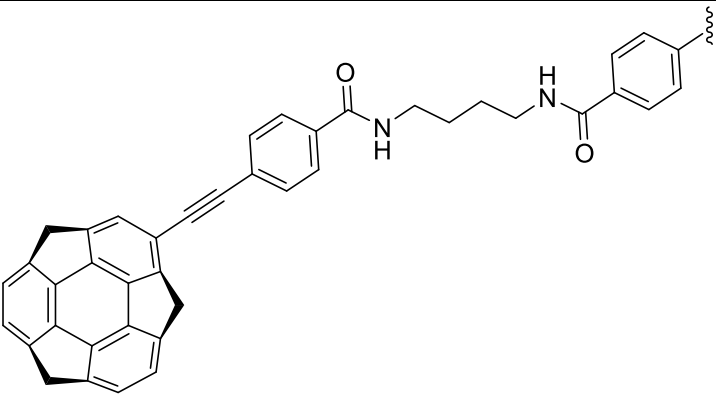
Fig. S15 The TGA curves (nitrogen atmosphere) of materials **6**, **8**, **10** and **11**.

The results of elemental analysis experiments for materials **6**, **8**, **10** and **11** are presented in **Table S1**. For the general comparison of the results, the structures of the introduced surface moieties in materials **6**, **8**, **10** and **11** together with the estimated contents (in at%) of elements C, H, N in those moieties, is also provided. The slight content of H in cobalt nanomagnets (**6**) results from the presence of adsorbed water. The content of nitrogen was found only in the samples of materials **10** and **11**, which contain nitrogen in the form of an amide bonds (materials **10**, **11**) or amide bonds and primary amino groups (material **10**). Judging from the structure of introduced moieties in materials **10** and **11**, the highest relative content (in at%) of nitrogen (among C, H, N) can be concluded in material **10**. This trend can be observed in the results of elemental analysis. The trend in the content of carbon (in at%) observed for the samples of materials **8**, **10** and **11** is in a good agreement with the trend of estimated relative carbon content (among C, H, N) in the structure of introduced moieties.

Table S1 The results of elemental analysis of materials **6**, **8**, **10** and **11**. The estimated relative contents (in at%) in the structure of introduced moieties is also given.

Material	N (at%)	C (at%)	N (at%)	Structure of the introduced surface moiety together with the estimated contents (in at%) of elements C, H, N in those moieties
6	-	2.66	0.25	-
8	-	11.67	1.02	Elemental Analysis (*ca.*): C, 69.42; H, 4.16
10	3.16	12.29	2.12	Elemental Analysis (*ca.*): C, 69.08; H, 7.91; N, 14.65;
11	1.37	21.01	1.54	Elemental Analysis (*ca.*): C, 84.66; H, 5.03; N, 4.82

Microscopic analyses (TEM, SEM) provided an insight in the morphology of material **11**. The TEM images of material **11** reveal the core-shell morphology of the resultant material together with the presence of few-layer carbon coating (**Fig. S16**). The presence of a non-uniform, thin layer covering the carbon surface of nanoparticles (marked with the blue arrow in **Fig. S16**) can be ascribed to the presence of introduced moieties of the surface. Interestingly, TEM with EDS-HAADF (energy-dispersive X-ray spectroscopy - high-angle annular dark-field technique) analyses suggest the relatively homogeneous surface modification of carbon layer of the nanoparticles, as visualised representatively for oxygen distribution over the carbon layer (cobalt distribution is also presented), see **Fig. S17**. Changes in morphology of the target material **11** in comparison to parent cobalt nanomagnets (**6**) can be also seen from SEM images (**Fig. S18**).
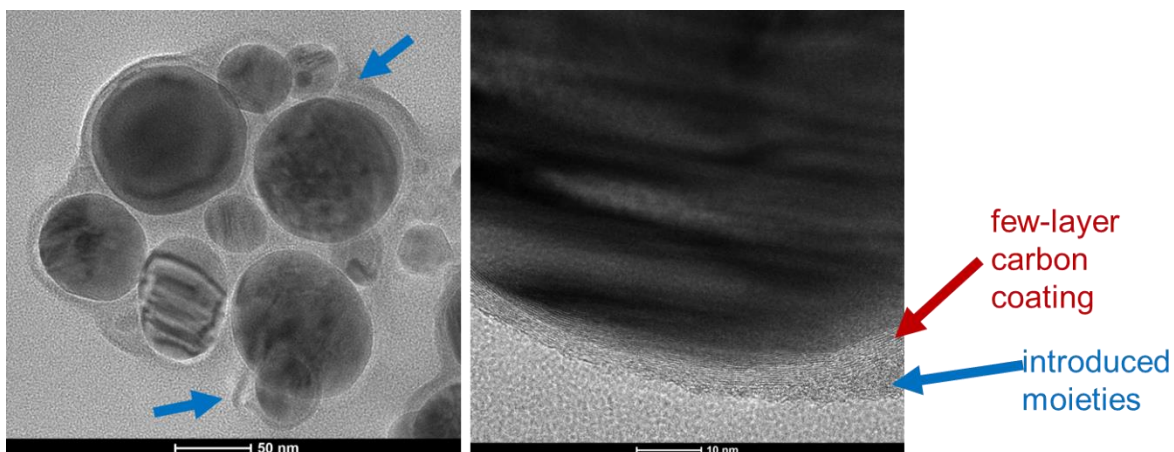
Fig. S16 TEM images of material **11** presented for different resolutions. The most essential parts that were ascribed to the introduced surface moieties are marked with blue arrows. The few-layer carbon coating is marked with brown arrow.
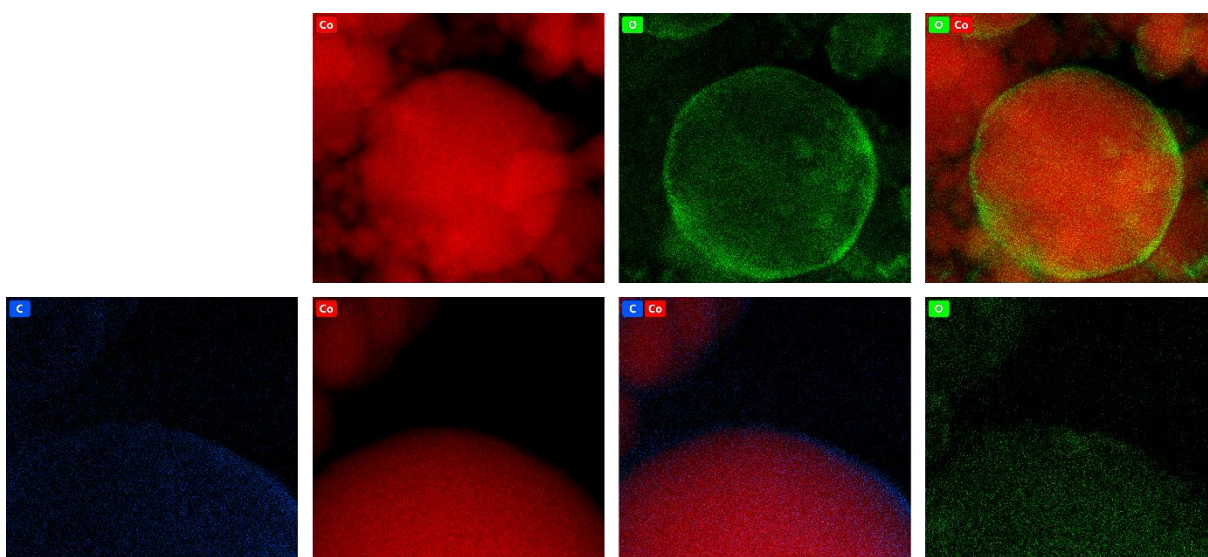

Fig. S17 EDS-HAADF-TEM images of material **11** presenting the distribution of elements in the particles.
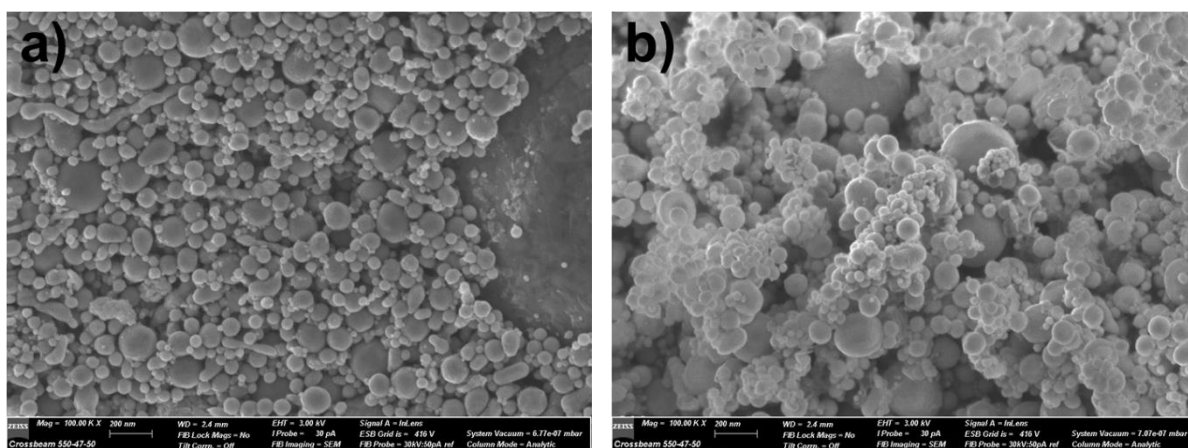

Fig. S18 SEM images of (**a**) cobalt nanomagnets **6** and (**b**) material **11**.

S3. Adsorption performance of the magnetic nanoadsorbent 11

S3.1. General procedure for the adsorption experiments

The magnetic nanoadsorbent **11** (10 mg) was added to 50 mL Falcon® tube containing the aqueous solution (10 mL) containing caesium (Cs) in the form of caesium chloride (CsCl) at a given concentration (100 mg/L, 80 mg/L, 40 mg/L, 20 mg/L, 10 mg/L, 8 mg/L, 5 mg/L, 1 mg/L). The mixture was shaken (600 rpm) for 30 minutes (the screening experiments were performed to investigate the optimal contact time, see **Fig. S20**). The magnetic nanoadsorbent was then separated from the reaction mixture by using a permanent neodymium magnet, and the supernatant was carefully removed with a glass Pasteur pipette. The supernatant was then filtered through a 0.25 μm syringe filter to a separate 15 mL Falcon® tube and subjected to ICP-MS/MS analysis. The concentration of Cs before the adsorption experiment was determined utilising ICP-MS/MS technique. All the adsorption tests were performed at room temperature. Additionally, the presence of adsorbed Cs on the surface of magnetic nanoadsorbent **11** was confirmed with SEM-EDS analysis (**Fig. S21**).

The results of DLS measurements (size distribution histograms, analyses in water) on the samples of cobalt nanomagnets **6**, the magnetic nanoadsorbent **11** and **11** with the adsorbed Cs salt are presented in **Fig. S22**. Additionally, surface zeta potential of the **11** with the adsorbed Cs was more negative (−28.7±1.1 mV) than for **11**, what was ascribed to the presence of Cs salt in the analysed sample. The DLS profile for this sample was similar to that of **11** (see size distribution histograms in **Fig. S22**).

The adsorption experiments with the Cs concentration of 100 mg/L were selected for the adsorbents' regeneration and re-use experiments. After the adsorption test and magnetic separation, the magnetic nanoadsorbent **11** was regenerated as follows:

1. It was dispersed in distilled water (0.5 mL) and sonicated for 10 minutes at 25°C.
2. The supernatant was precisely removed.
3. The material was once again dispersed in distilled water (0.5 mL) and sonicated for 10 minutes at 25°C.
4. The supernatant was precisely removed, and the material was dried at 45°C for 24 hours.

The magnetic nanoadsorbent **11** was then used in the next adsorption cycles. The results are ssummarised in **Fig. S23**. The regeneration of the magnetic nanoadsorbent **11** was supported with FT-IR spectroscopy which showed no significant differences in the spectra profiles before the adsorption process and after the regeneration process (**Fig. S24**), as well as TEM microscopy which showed no significant morphological changes between these samples (**Fig. S25**). Elemental analyses also supported the formation of **11**, as the data before (Found: N, 1.37; C, 21.01; H, 1.54) and after (N, 1.36; C, 20.98; H, 1.57) adsorption and regeneration, were highly consistent.

Similar adsorption studies were performed for Na$^+$ and K$^+$ as representative interferents. The experiments were performed for (a) the solution containing only the given metal (Cs, Na, K, Ba, Ni) or (b) the removal of Cs was tested in the presence of

Na, K, Ba, Ni (mixture of salts was subjected to this experiment). The results of these tests are presented in **Fig. S26**.

Each adsorption experiment was repeated three times to check the reproducibility of the results.

The adsorption process (**Fig. S19**) tends to follow the Langmuir adsorption model.[7,8] The parameters, such as the maximum adsorption capacity ($Q_{e\,max}$) and Langmuir constant (K_L) were estimated by applying the linear equation (**Fig. S27**) of the Langmuir isotherm model (1)[7,8]:

$$\frac{C_e}{Q_e} = \frac{C_e}{Q_{e\,max}} + \frac{1}{K_L \cdot Q_{e\,max}} \qquad (1)$$

In this equation (1) here K_L is the Langmuir constant (L/g), $Q_{e\,max}$ is the maximum adsorption capacity (mg/g), C_e is the analyte (Cs) concentration at the equilibrium (mg/L), Q_e is the analyte (Cs) uptake capacity (mg/g). The R^2 of the linear regression was *ca.* 0.994. Q_{emax} parameter was taken as $\frac{1}{\text{slope}}$, whilst K_L parameter was taken as $\frac{1}{\text{intercept} \cdot Q_{e\,max}}$.

The comparison of the maximum adsorption capacity value for the magnetic nanoadsorbent **11** and reported adsorbents is listed in **Table S2**.

Similar adsorption test was performed for native cobalt nanomagnets **6** to compares Cs removal efficiency between magnetic nanoadsorbent **11** and native cobltn nanoparticles **6**. The results of this test are presented in **Fig. S28** and **Fig. S29**. The respective Cs adsorption test with the native cobalt nanomagnets **6** revealed that the Q_{emax} value for **6** is *ca.* 4.4 mg/g. This value is consistent with the literature data on the removal of other metal cations with the similar carbon-encapsulated magnetic nanoparticles[9], and is significantly lower than for the magnetic nanoadsorbent **11**.

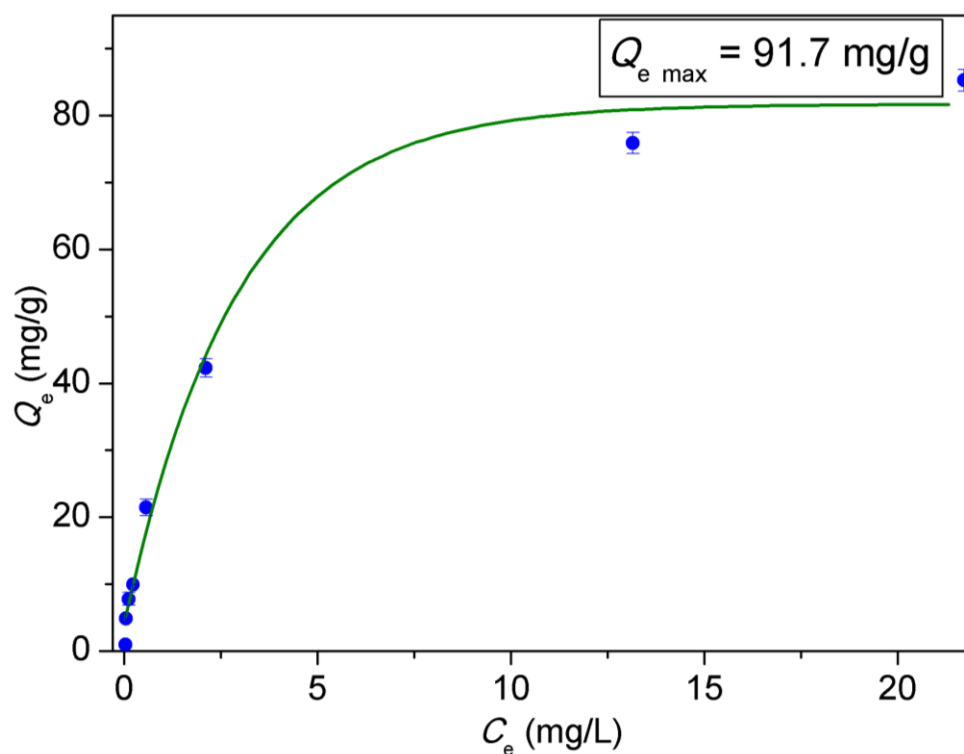## S3.2. Data on the adsorption experiments

Fig. S19 Adsorption isotherm of Cs adsorption with the magnetic nanoadsorbent **11**. The Langmuir model fitting is also presented.
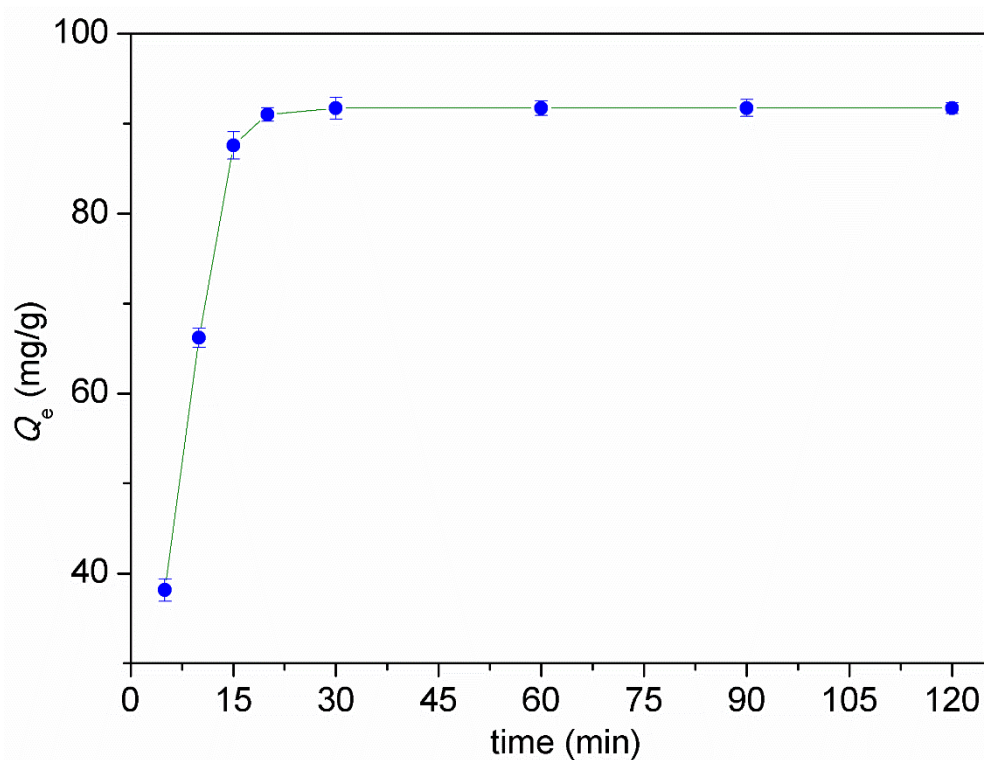

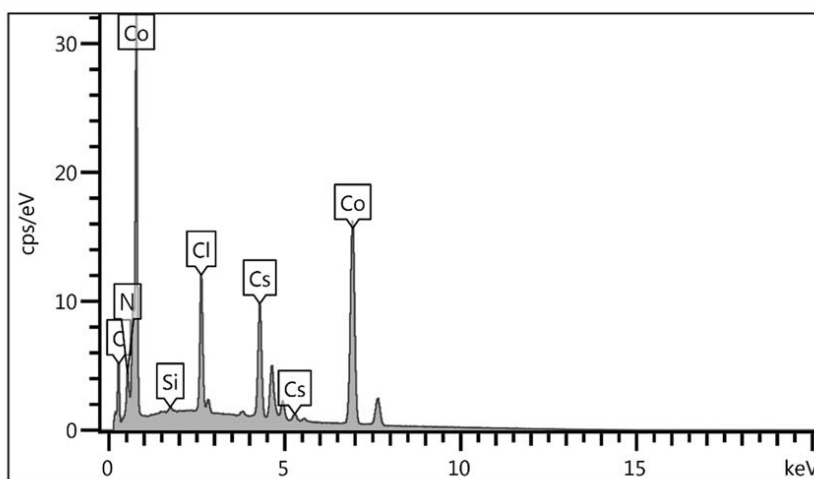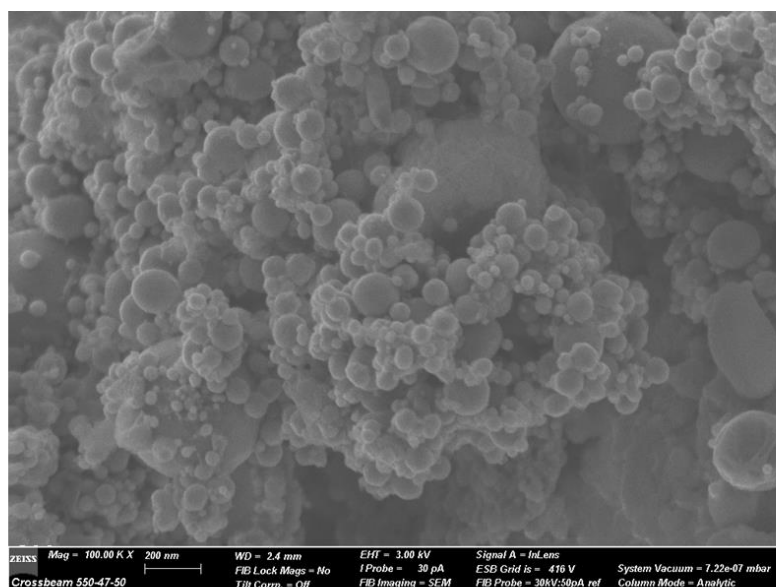**Fig. S20** Effect of time on removal efficiency with the magnetic nanoadsorbent **11**.
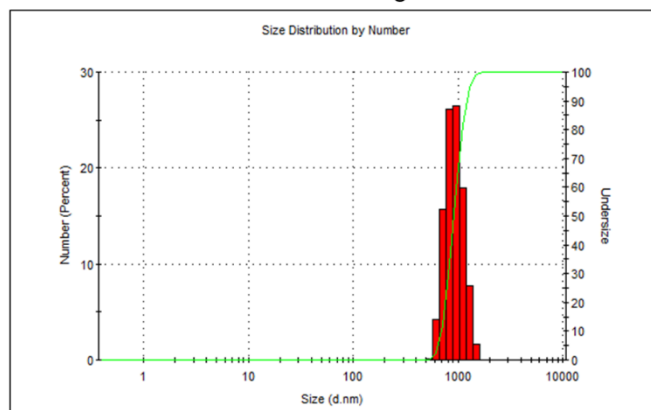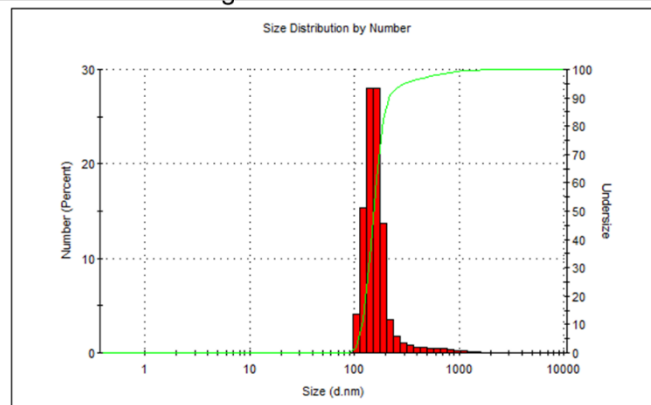
Fig. S21 SEM-EDS analyses on the magnetic nanoadsorbent **11** after the Cs and before the regeneration., whowing the presence of adsorbed Cs on the surface of the material.

cobalt nanomagnets **6**

magnetic nanoadsorbent **11**

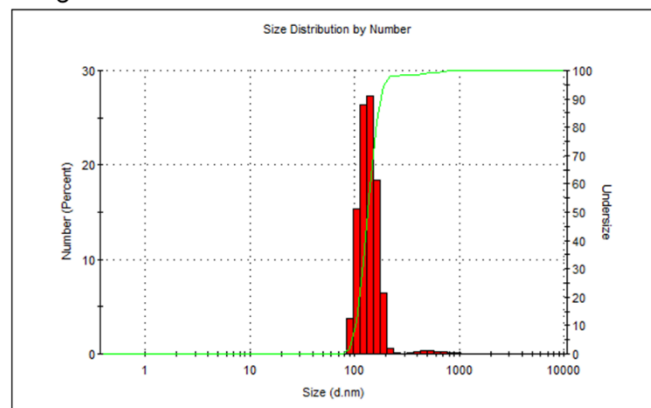magnetic nanoadsorbent **11** with the adsorber Cs salt

Fig. S22 Size distribution histograms (by number) obtained from DLS analyses (in water).
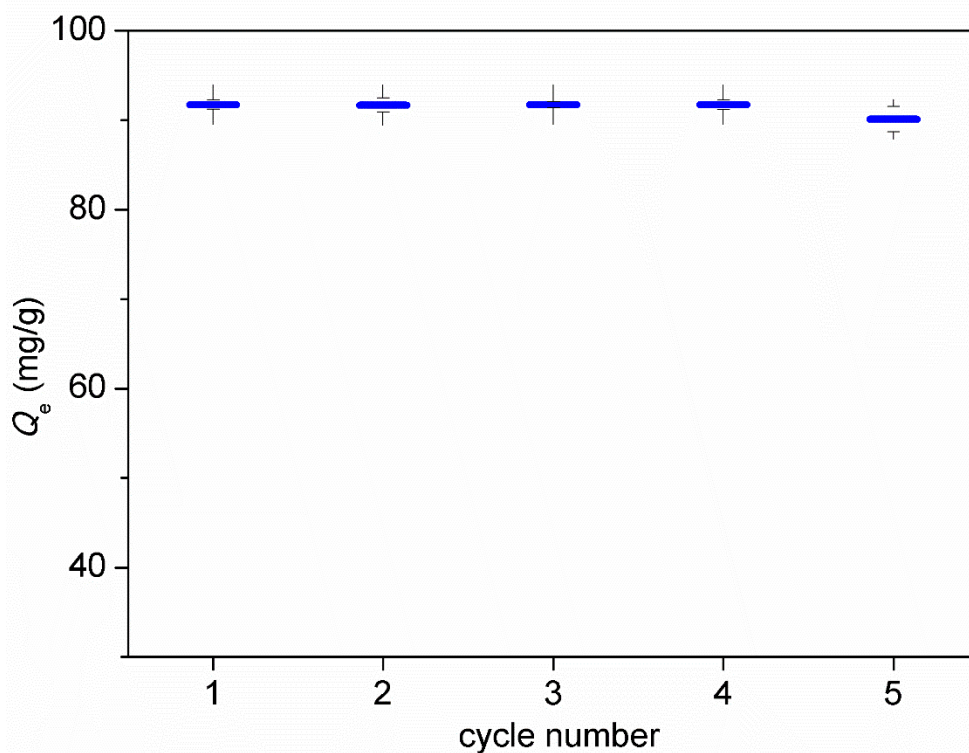
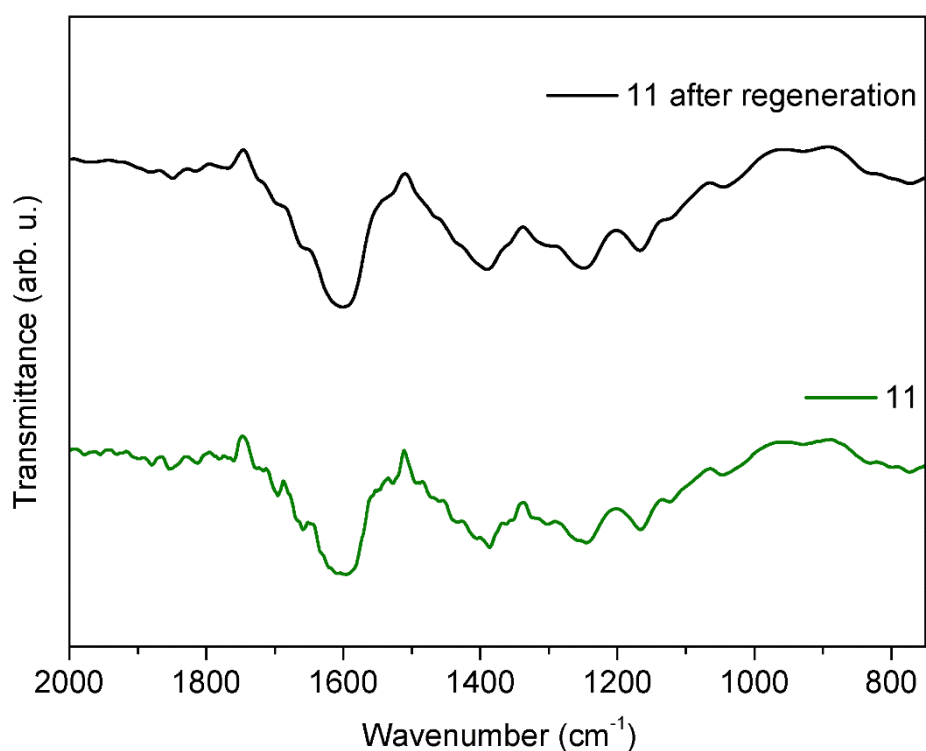**Fig. S23** Reusability studies on the magnetic nanoadsorbent **11**.

Fig. S24 FT-IR (KBr) spectra of magnetic nanoadsorbent **11** after (black curve) the regeneration from the adsorption process and before (green curve) the adsorption process, showing no significant differences in the spectra profiles.
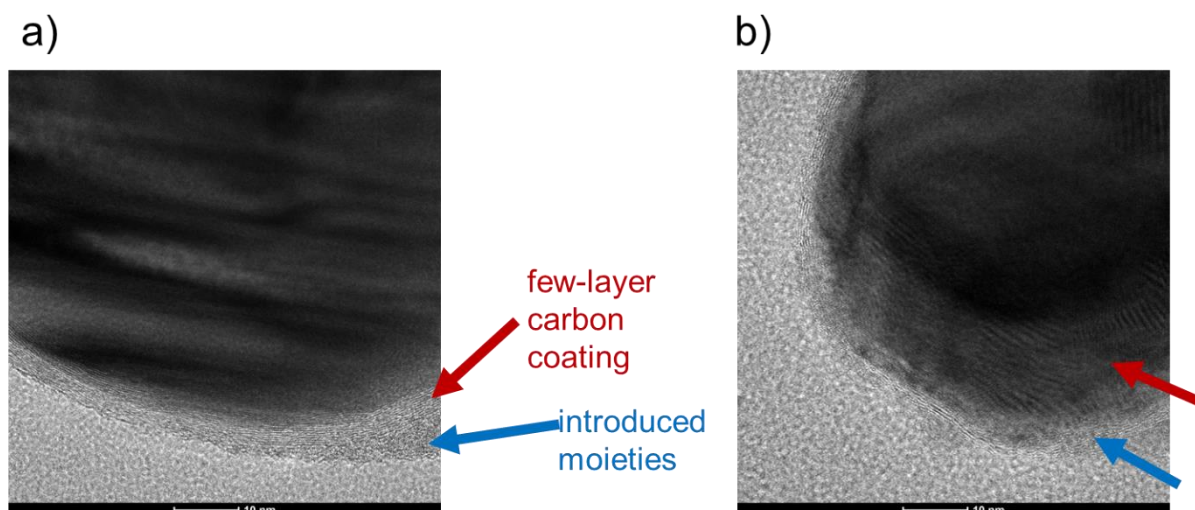
Fig. S25 TEM images of material **11** **(a)** before the adsorption process, **(b)** after the regeneration process after the adsorption, showing no significant morphological changes between the samples.
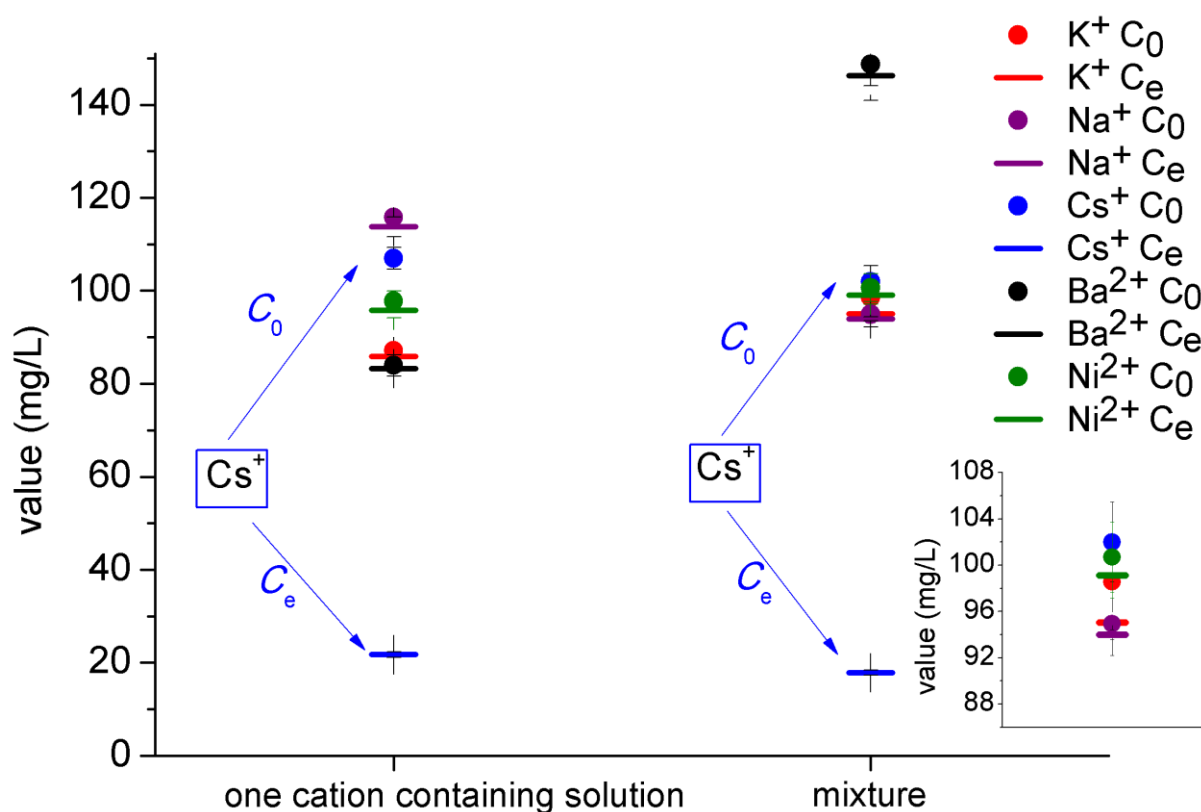

Fig. S26 Selectivity studies on the magnetic nanoadsorbent **11**. The inset for the analysis of the mixture (removal Cs in the presence of Na, K, Ba, Ni) is also presented.
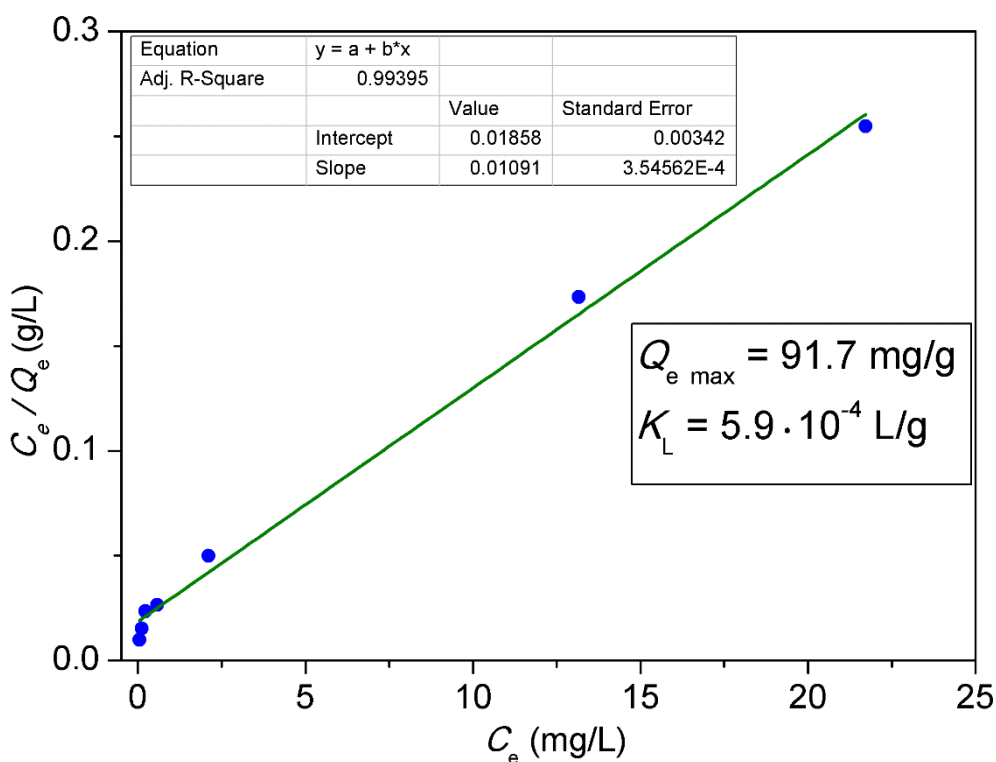
Fig. S27 Linear fit of the experimental data for the adsorption test with magnetic nanadsorbent **11** using the Langmuir isotherm model.

Table S2 Comparison of the data of maximum adsorption capacity for the magnetic nanoadsorbent **11** and reported Cs adsorbents.

Adsorbent	Maximum adsorption capacity $(mg \cdot g^{-1})$	Reference
geological mineral adsorbents	1.86 - 35.77	10
graphene oxide[a]	180 - 465	11
metal-organic frameworks (MOFs)[b]	23.43 - 36.47	12
crown ether- or calixarene-based materials[c]	26.98 - 107.16	13-14
various biosorbents[c]	4.94 - 208.0	15
Carbon-nanotubes based materials[c]	12.75 - 142.85	15
Prussian Blue containing magnetic adsorbents[a]	16.2 - 96	16,17
magnetic nanoadsorbent 11	**91.7**	**This work**

[a] for this material low Cs-selectivity of adsorption was concluded, especially in the case of Mg as competitive interferent; [b] the competing removal of Sr was also concluded; [c] the compering effect of especially Na and K was concluded for the selected materials, see data in papers[14-15].
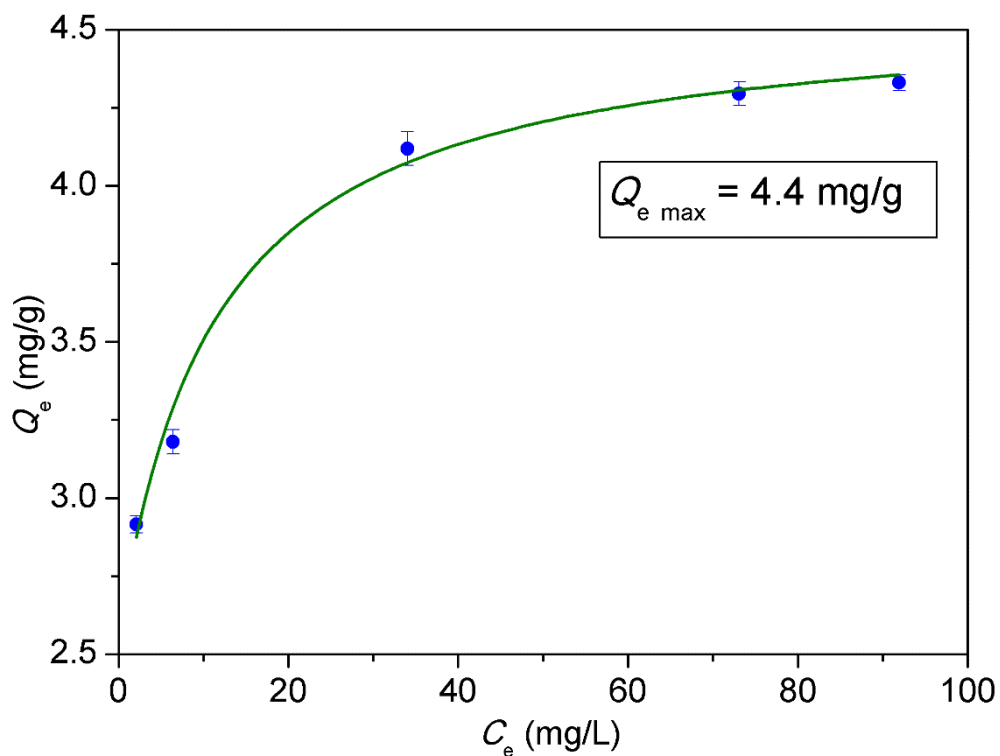
Fig. S28 Adsorption isotherm of comparative Cs adsorption with the native cobalt nanomagnets **6**. The Langmuir model fitting is also presented.
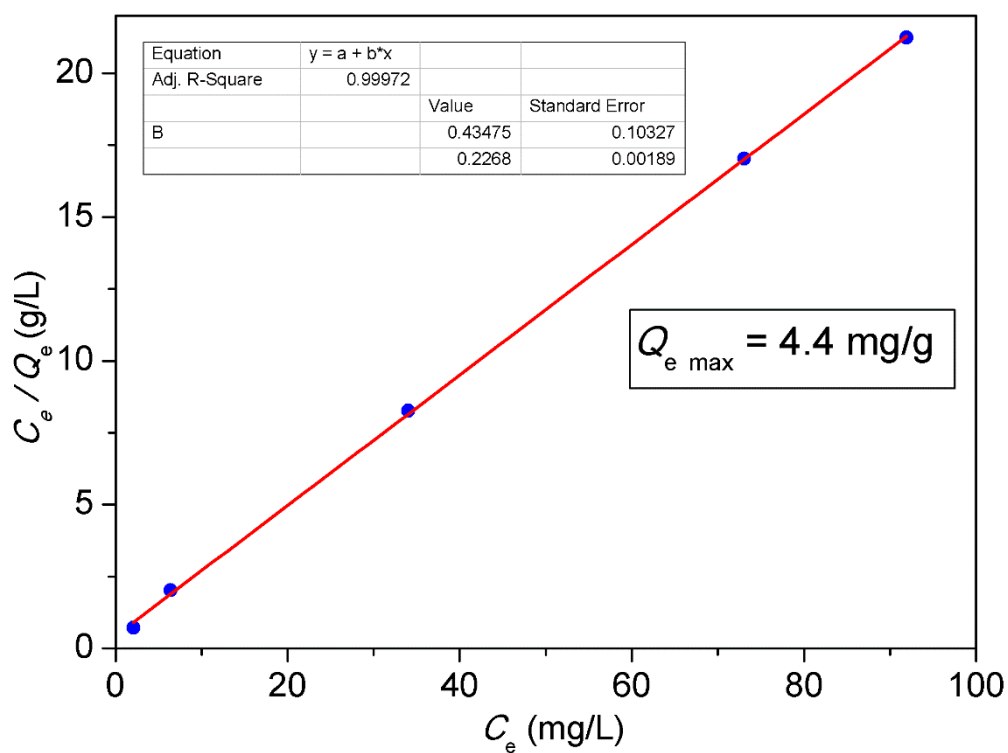

Fig. S29 Linear fit of the experimental data for the comparative adsorption test with the native cobalt nanomagnets **6** using the Langmuir isotherm model.

S4. Application of the magnetic nanoadsorbent 11 for the removal of caesium salts from the aqueous wastes in the synthesis of (*R,E*)-*N*-(2,5-difluorobenzylidene)-2-methylpropane-2-sulfinamide 14, a starting material for the synthesis of larotrectinib®

S4.1. General procedure for the adsorption experiments
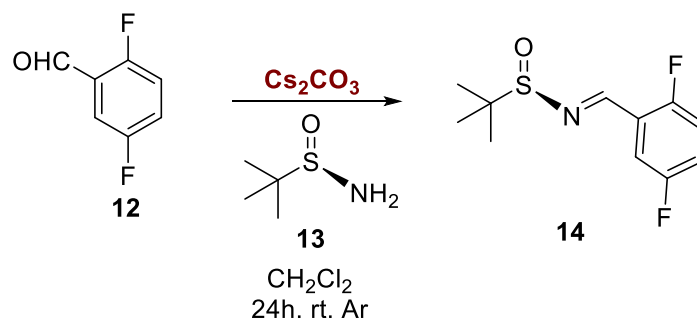

Fig. S30 The synthesis of (*R,E*)-N-(2,5-difluorobenzylidene)-2-methylpropane-2-sulfinamide **14**, a starting material for the synthesis of larotrectinib®.

To generate the Cs (in the form of caesium carbonate, Cs_2CO_3) containing aqueous waste, the synthesis of compound **14** was performed (**Fig. S30**), employing the reported procedure[18]:

*A solution of 2,5-difluorobenzaldehyde (**12**; 5 µL, 6.1 mg, 0.043 mmol), (R)-2-methylpropane-2-sulfinamide (**13**; 5.5 mg, 0.045 mmol) and Cs_2CO_3 (9.8 mg, 0.030 mmol) in dry DCM (3 mL) was stirred for 24 hours at room temperature under argon atmosphere. The reaction mixture was diluted with DCM (20 mL) and washed with distilled water (2 x 10 mL = 20 mL). Water layer was collected and used for the adsorption tests. Combined organic layers were dried over $MgSO_4$. After filtration, volatiles were distilled off using a rotary evaporator.*

To instigate the action of the magnetic nanoadsorbent **11**, the material (100 mg) was added to a 50 mL Falcon® tube containing the as-generated Cs containing aqueous waste. The mixture was shaken (600 rpm) for 30 minutes. The magnetic nanoadsorbent was then separated from the reaction mixture using a permanent neodymium magnet, and the supernatant was carefully removed with a glass Pasteur pipette. The supernatant was then filtered through a 0.25 µm syringe filter to a separate 15 mL Falcon® tube and subjected to ICP-MS analysis. The concentration of Cs before the adsorption experiment was determined by the ICP-MS/MS technique. The content of Cs in the solid adsorbent **11** was also checked employing ICP-MS/MS (after the precise removal of the supernatant, the solid material was dried at 45°C for 24 hours). All the adsorption tests were performed at room temperature.

The synthesis of compound **14** and, in consequence, each adsorption experiment was repeated three times to check the reproducibility of the results. The ¹H

NMR spectra of crude mixture comprising compound **14** were highly consistent with each other, see the ^{1}H NMR spectra in **Fig. S31**-**Fig. S33**.The results of the adsorption experiments are summarised in **Fig. S34**.

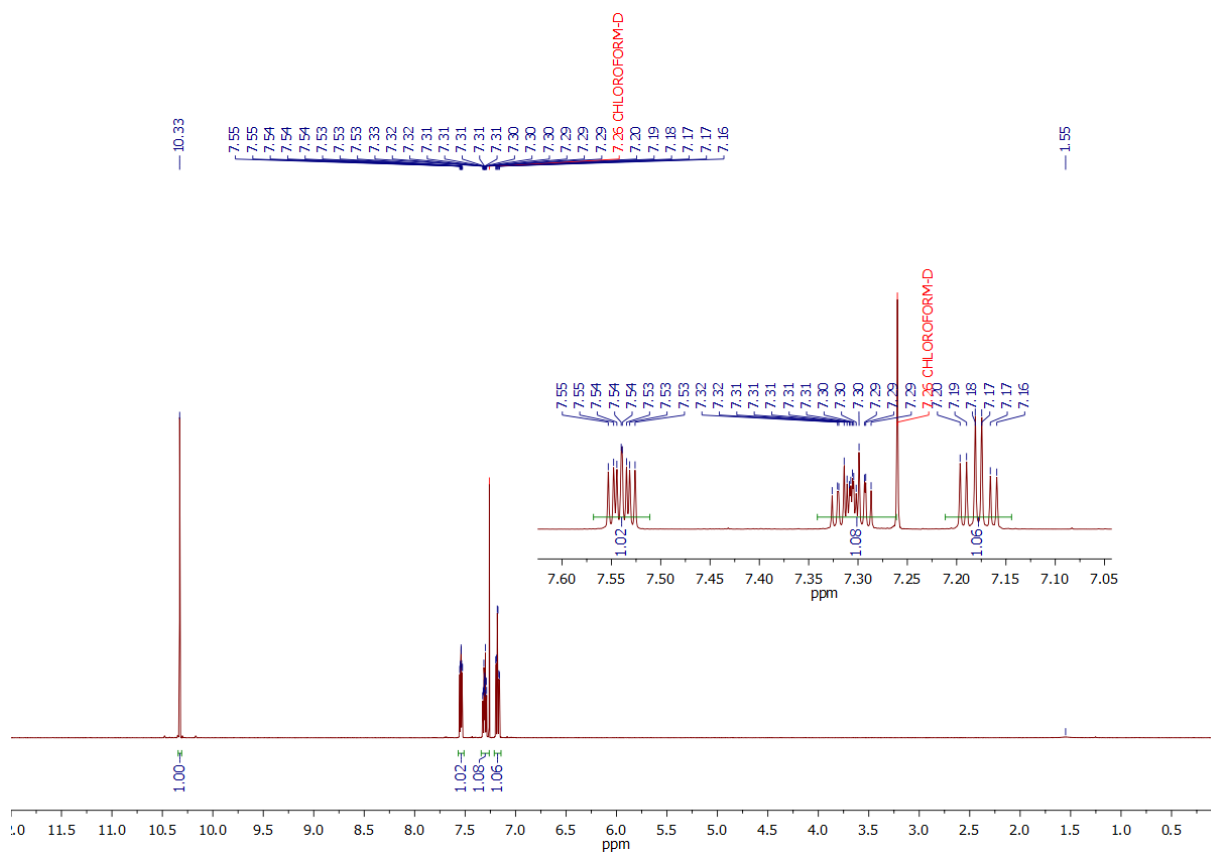## S4.2. Data on the adsorption experiments

Fig. S31 ^{1}H NMR (CDCl$_3$, 500 MHz) of **12**.
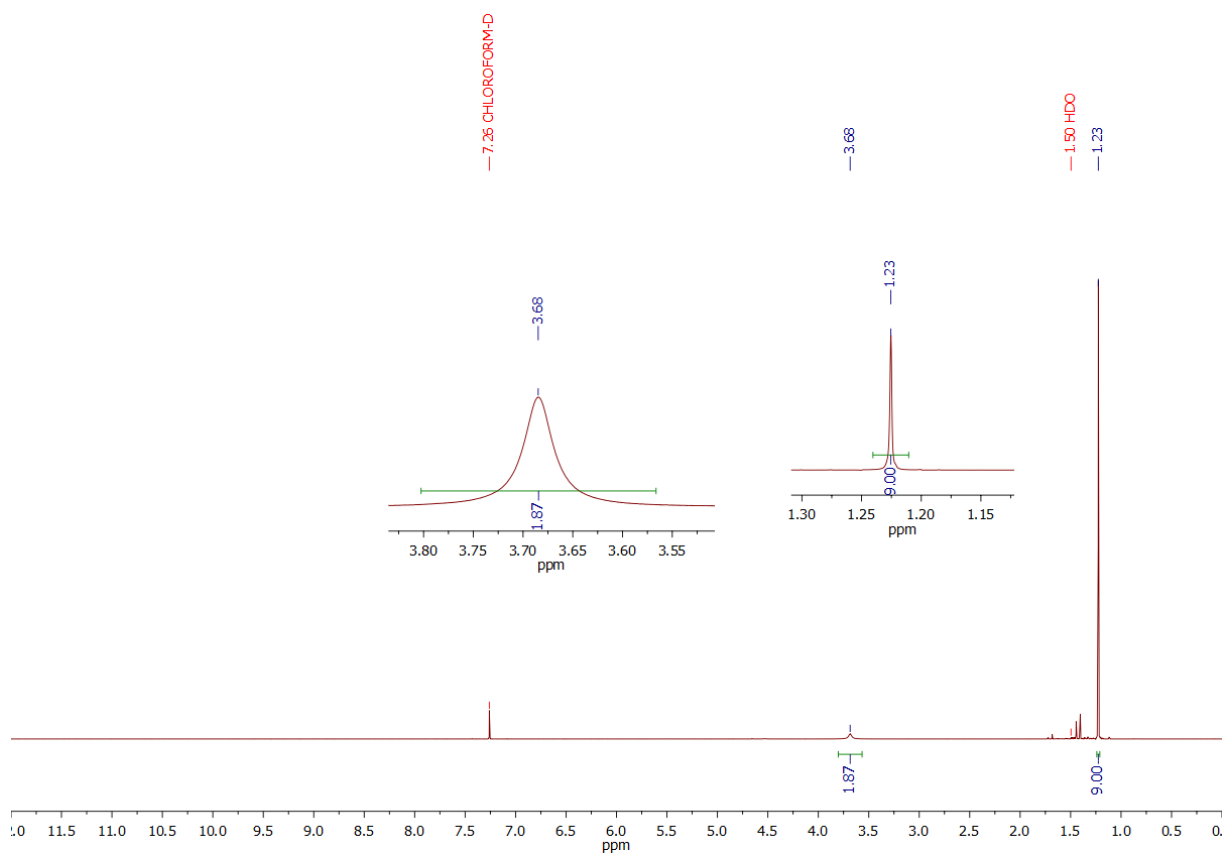
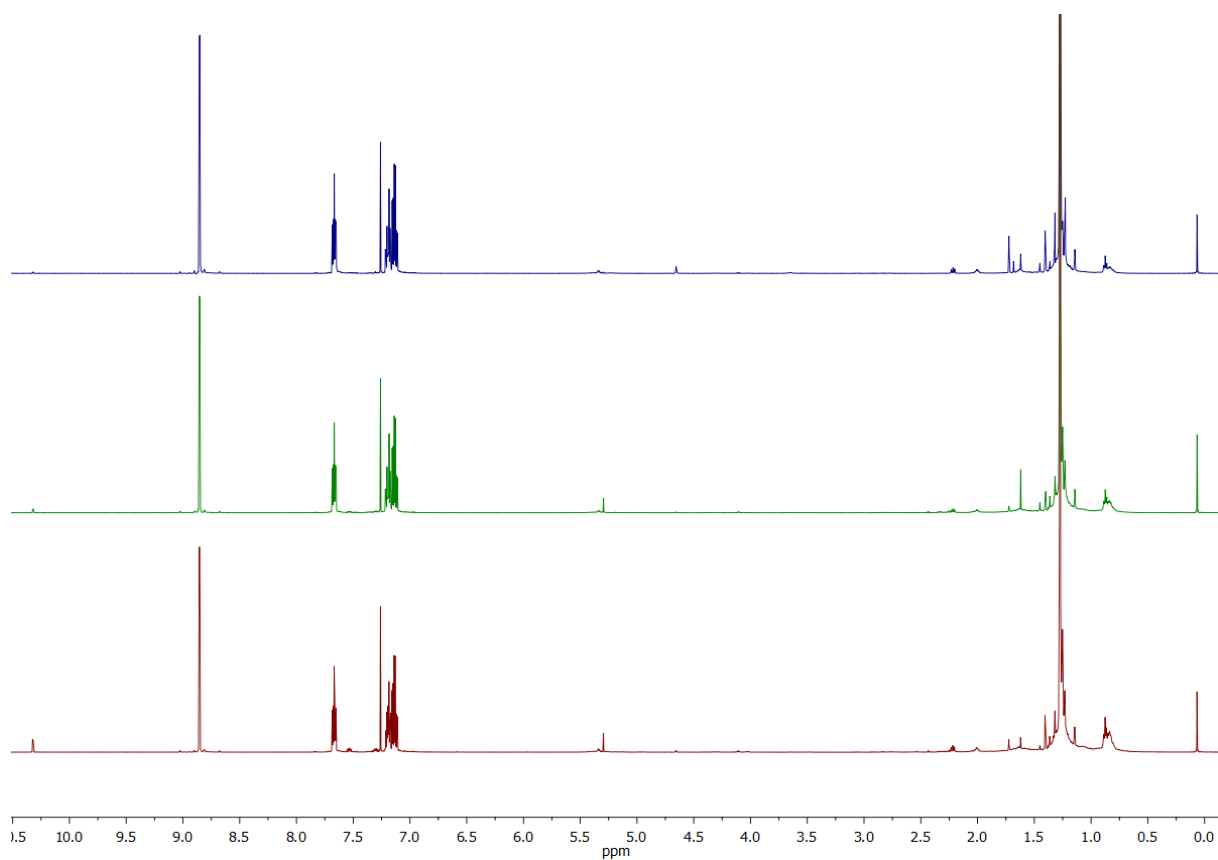**Fig. S32** ^{1}H NMR (CDCl$_3$, 500 MHz) of **13**.

Fig. S33 ^{1}H NMR (CDCl$_3$, 500 MHz) of the crude mixture containing **14** (stacked spectra are presented). The spectra from three independent syntheses are presented.
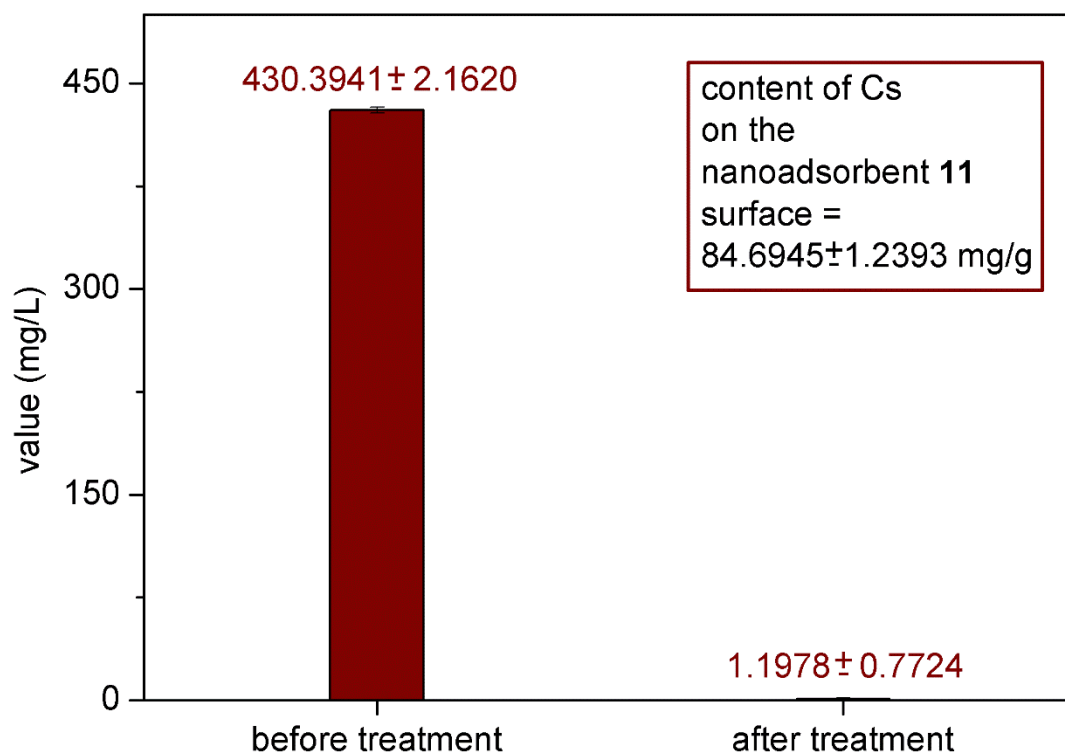
Fig. S34 Performance of the magnetic nanomaterial **11** towards the removal of Cs from the aqueous waste from the synthesis of **14**.

S5. Application of the magnetic nanoadsorbent 11 for the removal of caesium salts from the aqueous wastes in the desilylation of (4-bromophenoxy)(*tert*-butyl)dimethylsilane 15

S5.1. General procedure for the adsorption experiments

Fig. S35 The desilylation of (4-bromophenoxy)(*tert*-butyl)dimethylsilane **15** to 4-bromophenol **16**

To generate the Cs (in the form of caesium fluoride, CsF) containing aqueous waste, the desilylation of compound **15** to 4-bromophenol **16** was performed (**Fig. S35**), as the representative process, employing the below procedure:

*A solution of (4-bromophenoxy)(tert-butyl)dimethylsilane (**15**; 7.5 µL, 8.8 mg, 0.031 mmol) and CsF (6.9 mg, 0.048 mmol) in dry CH₃OH (2 mL) was stirred for 5 hours at room temperature under argon atmosphere. The reaction mixture was diluted with ethyl acetate (20 mL) and washed with distilled water (2 x 10 mL = 20 mL). Water layer was collected and used for the adsorption tests. Combined organic layers were dried over MgSO₄. After filtration, volatiles were distilled off using a rotary evaporator.*

To instigate the action of the magnetic nanoadsorbent **11**, the material (75 mg) was added to 50 mL Falcon® tube containing the as-generated Cs containing aqueous waste. The mixture was shaken (600 rpm) for 30 minutes. The magnetic nanoadsorbent was then separated from the reaction mixture by using a permanent neodymium magnet, and the supernatant was carefully removed with a glass Pasteur pipette. The supernatant was then filtered through a 0.25 µm syringe filter to a separate 15 mL Falcon® tube, and subjected to ICP-MS/MS analysis. The concentration of Cs before the adsorption experiment was also determined by ICP-MS/MS technique. In addition, the content of Cs in the solid adsorbent **11** was also checked using ICP-MS/MS (after the precise removal of the supernatant, the solid material was dried at 45°C for 24 hours). All the adsorption tests were performed at room temperature.

The synthesis of compound **16** and, in consequence, each adsorption experiment was repeated three times to check the reproducibility of the results. The ¹H NMR spectra of crude mixture comprising compound **16** were highly consistent with each other, see the ¹H NMR spectra in **Fig. S36**-**Fig. S37**. The results of the adsorption experiments are summarised in **Fig. S38**.

S5.2. Data on the adsorption experiments
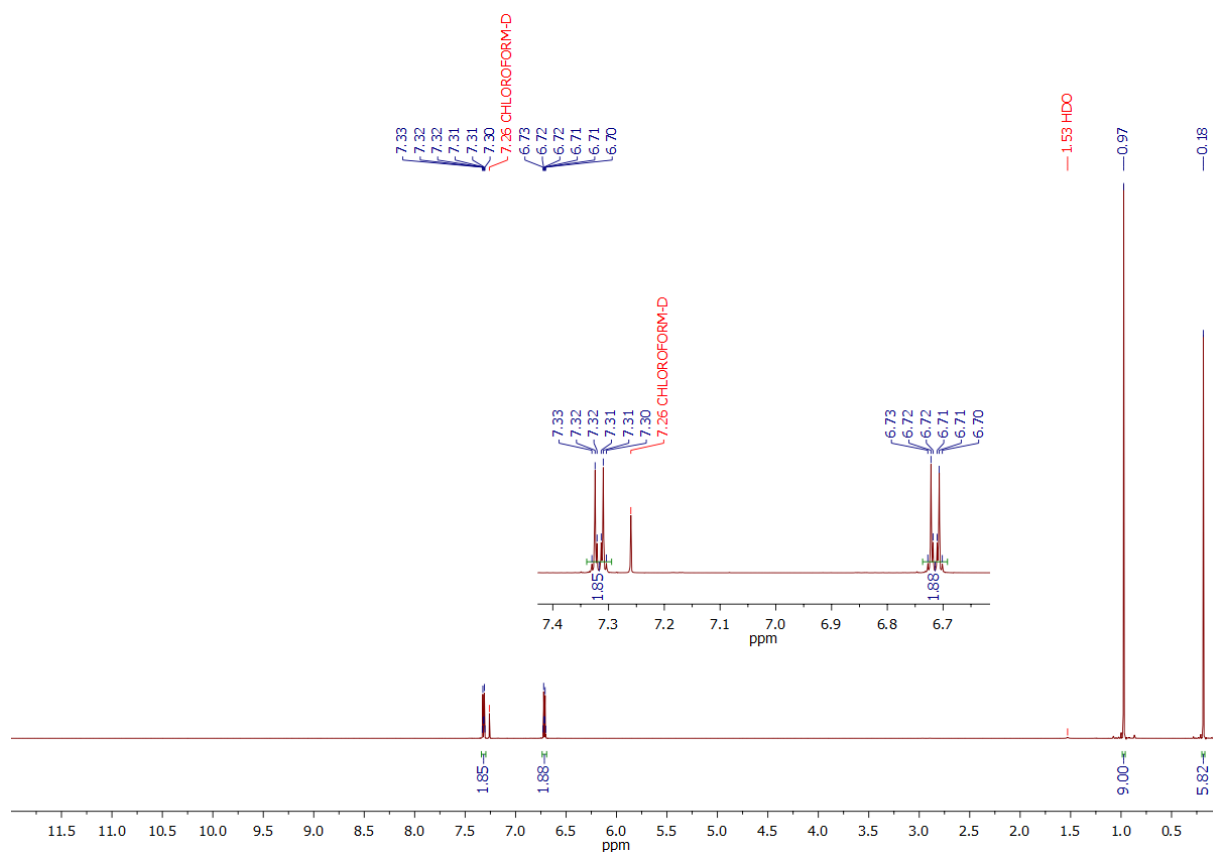

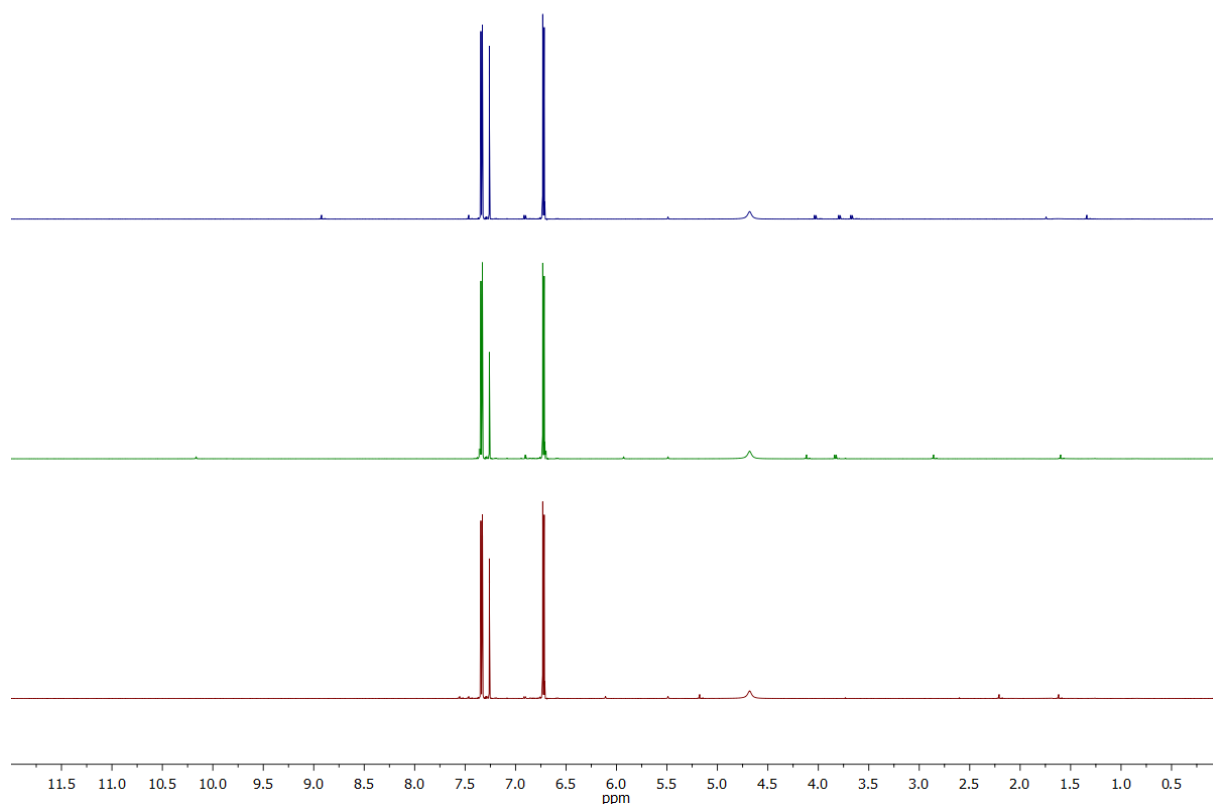**Fig. S36** ^{1}H NMR (CDCl$_3$, 500 MHz) of **15**.

Fig. S37 ^{1}H NMR (CDCl$_3$, 500 MHz) of the crude mixture containing **16** (stacked spectra are presented). The spectra from three independent syntheses are presented.
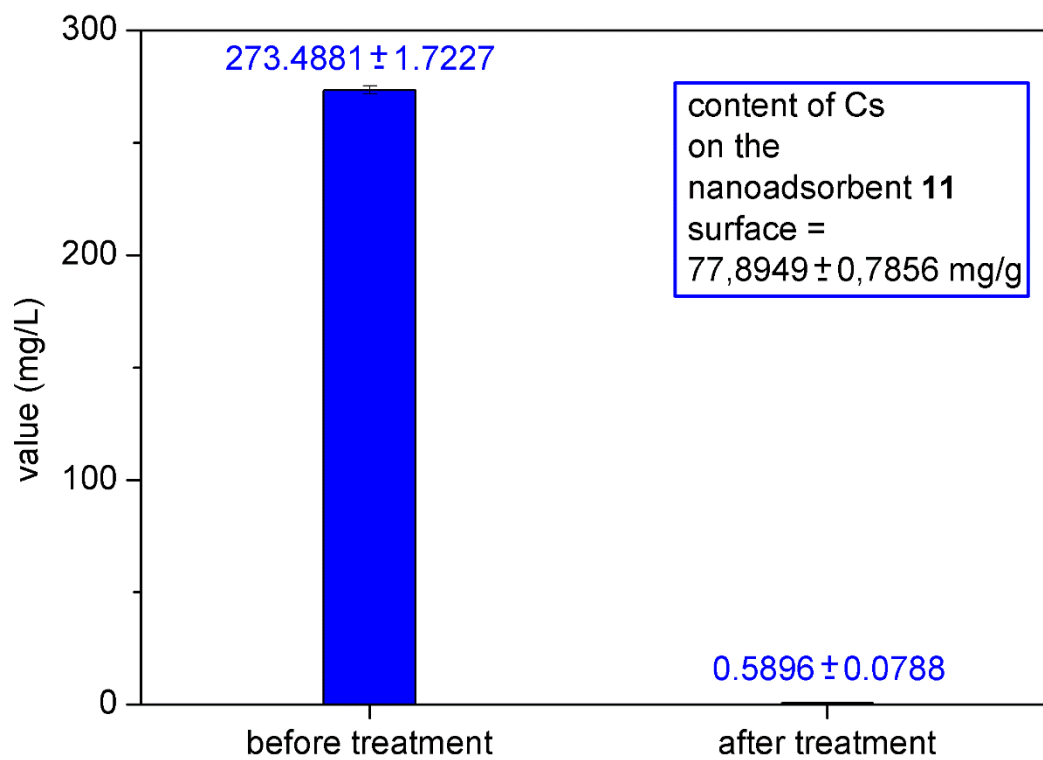
Fig. S38 Performance of the magnetic nanomaterial **11** towards the removal of Cs from the aqueous waste from the synthesis of **16**.

S6. Investigation of the supramolecular interactions between sumanene (1) and Cs⁺.

The interactions between native sumanene (**1**) and caesium cations (Cs^+) in the form of cesium hexafluorophosphate ($CsPF_6$) were probed with emission spectra titration assay. The experiments were performed in the 1:1 *v/v* mixture of tetrahydrofuran (THF) and distilled water (H_2O). Further portions (10-20 µL) of stock solutions of $CsPF_6$ ($1.5 \cdot 10^{-3}$ M or $6.0 \cdot 10^{-3}$ M) in THF:H_2O 1:1 *v/v* were added to the solution of sumanene ($2 \cdot 10^{-5}$ M) in THF:H_2O 1:1 *v/v* (3 mL) to reach given receptor-to-cation molar ratio. The excitation wavelength was 280 nm, whilst the data for calculations were collected for the emission intensity at $\lambda_{em} =$ 380 nm. The results of the titration experiment are presented in **Fig. S39.** Increasing the amount of Cs^+ caused an increase in sumanene's emission intensity. The changes between each intervals were not the same (**Fig. S40**) what was the result of complex stoichiometry.

Complex stoichiometry (sumanene:Cs^+) was investigated with the Job's plot method (continuous variation method).[19,20] The estimated complex stoichiometry was taken as the x_{Cs+} for the maximum value in the Job's plot (**Fig. S41**). The found complex stoichiometry (sumanene:Cs^+=2:1; $x_{Cs+,max}$=1/3) supported the formation of sandwich-type complexes, what is consistent with the previous conclusions for the interactions between Cs^+ and reported sumanene derivatives.[2,21–25]

The apparent binding constant (K_{app}) of the system was estimated using the Benesi-Hildebrand method[26,27], which is based on the equation:

$$\frac{1}{I - I_0} = \frac{1}{a} + \frac{1}{a \cdot K_{app} \cdot C(Cs^+)}$$

where I_0 and I are the fluorescence intensities of sumanene ($\lambda_{em} = 380$ nm) in the absence and presence of Cs^+, respectively, a is a constant, and $C(Cs^+)$ is the concentration of Cs^+ in solution. K_{app} was taken as a ratio of intercept-to-slope of $1/(I - I_0)$ vs. $1/C(Cs^+)$ linear plot (**Fig. S42**). The calculated value was 6.6×10^5 M^{-2}.
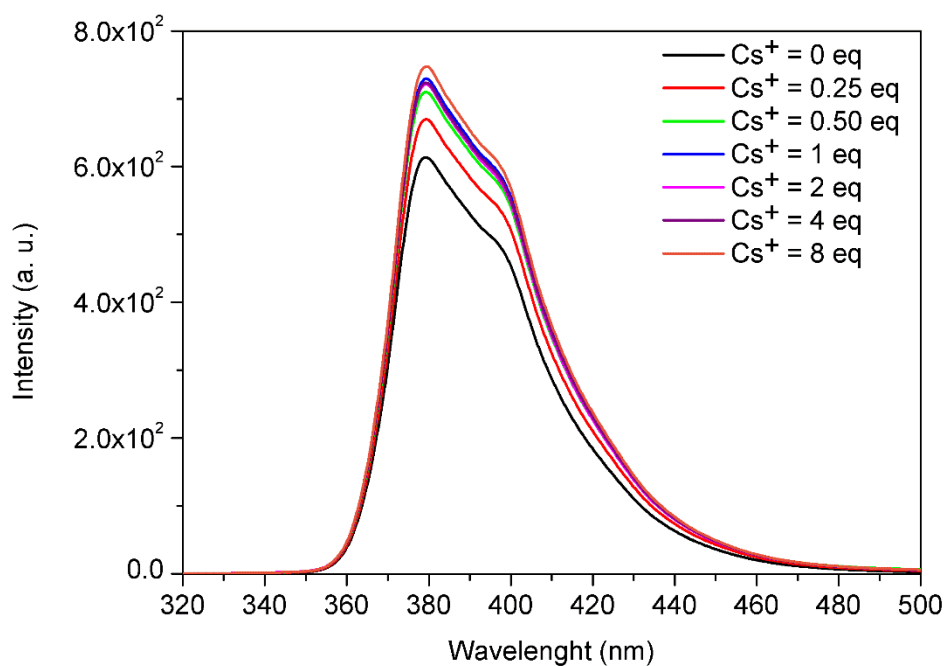
Fig. S39 Emission spectra titration assay with sumanene (**1**) and Cs^+ (THF:H_2O=1:1 *v/v*, $2 \cdot 10^{-5}$ M, λ_{ex} = 280 nm).
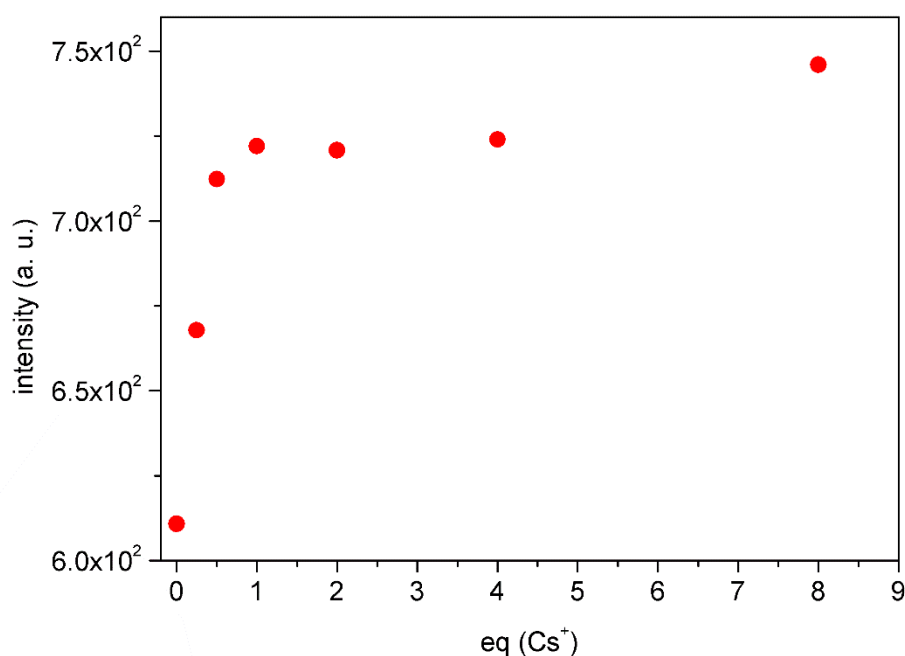

Fig. S40 Changes in the emission intensity of sumanene (**1**) upon the addition of further portions (molar eqivalents) of Cs^+.
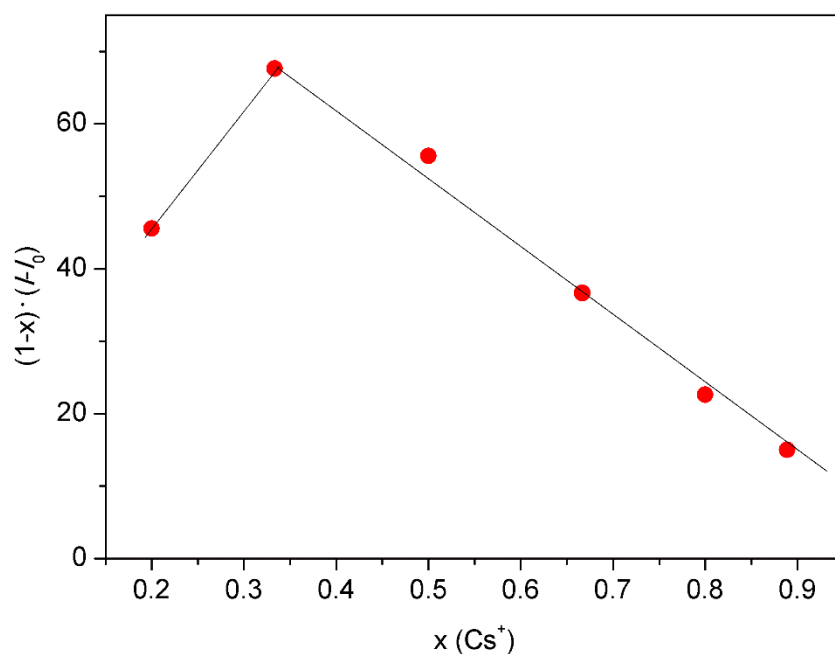
Fig. S41 The Job's plot for the estimation of complex stoichiometry for interactions between sumanene (**1**) and Cs^+.
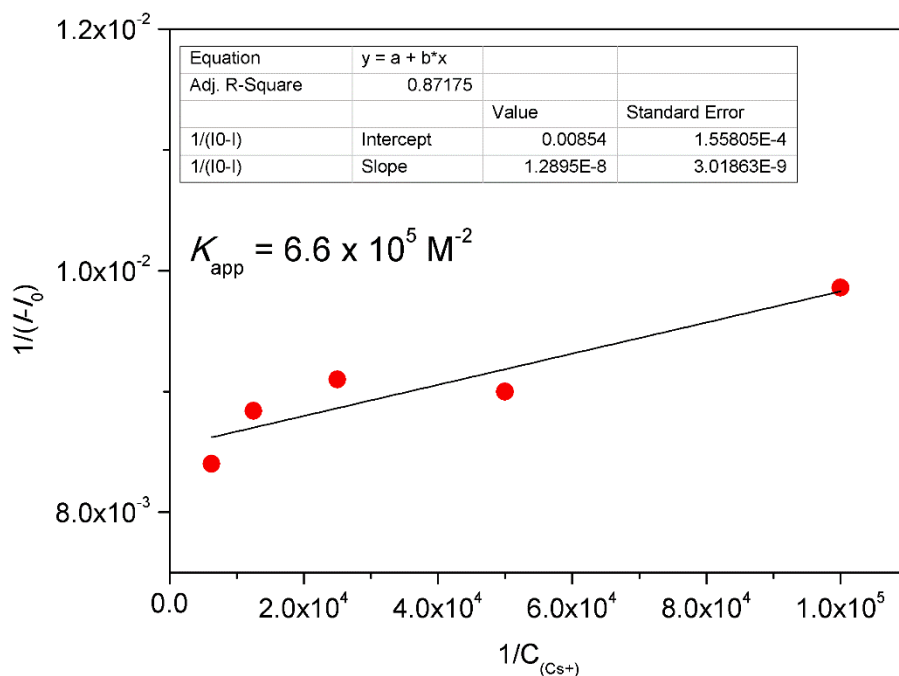

Fig. S42 Benesi-Hildebrand plot for the estimation of K_{app} for the interactions between sumanene (**1**) and Cs^+. The calculated K_{app} and the data are also presented.

S7. Supporting references

1   H. Sakurai, T. Daiko and T. Hirao, *Science*, 2003, **301**, 1878–1878.
2   A. Kasprzak, A. Gajda-Walczak, A. Kowalczyk, B. Wagner, A. M. Nowicka, M. Nishimoto, M. Koszytkowska-Stawińska and H. Sakurai, *J. Org. Chem.*, 2023, **88**, 4199–4208.
3   A. Schätz, T. R. Long, R. N. Grass, W. J. Stark, P. R. Hanson and O. Reiser, *Adv. Funct. Mater.*, 2010, **20**, 4323–4328.
4   R. N. Grass, E. K. Athanassiou and W. J. Stark, *Angew. Chem. Int. Ed.*, 2007, **46**, 4909–4912.
5   R. Fuhrer, I. K. Herrmann, E. K. Athanassiou, R. N. Grass and W. J. Stark, *Langmuir*, 2011, **27**, 1924–1929.
6   C. G. Tan and R. N. Grass, *Chem. Commun.*, 2008, 4297.
7   I. H. Ali, M. K. Al Mesfer, M. I. Khan, M. Danish and M. M. Alghamdi, *Processes*, 2019, **7**, 217.
8   H. Swenson and N. P. Stadie, *Langmuir*, 2019, **35**, 5409–5426.
9   P. Strachowski, W. Kaszuwara and M. Bystrzejewski, *New J. Chem.*, 2017, **41**, 12617–12630.
10   S. Kwon, Y. Kim and Y. Roh, *Sci Rep*, 2021, **11**, 15362.
11   P. Kaewmee, J. Manyam, P. Opaprakasit, G. T. Truc Le, N. Chanlek and P. Sreearunothai, *RSC Adv.*, 2017, **7**, 38747–38756.
12   B. Aguila, D. Banerjee, Z. Nie, Y. Shin, S. Ma and P. K. Thallapally, *Chem. Commun.*, 2016, **52**, 5940–5942.
13   Md. R. Awual, *Chemical Engineering Journal*, 2016, **303**, 539–546.
14   J. Wang and S. Zhuang, *Nucl. Eng. Technol.*, 2020, **52**, 328–336.
15   X. Liu, G.-R. Chen, D.-J. Lee, T. Kawamoto, H. Tanaka, M.-L. Chen and Y.-K. Luo, *Biores. Technol.*, 2014, **160**, 142–149.
16   T. Sasaki and S. Tanaka, *Chem. Lett.*, 2012, **41**, 32–34.
17   C. Thammawong, P. Opaprakasit, P. Tangboriboonrat and P. Sreearunothai, *J. Nanopart. Res.*, 2013, **15**, 1689.
18   H. Mei, J. Han, S. Fustero, M. Medio-Simon, D. M. Sedgwick, C. Santi, R. Ruzziconi and V. A. Soloshonok, *Chem. Eur. J.*, 2019, **25**, 11797–11819.
19   J. S. Renny, L. L. Tomasevich, E. H. Tallmadge and D. B. Collum, *Angew. Chem. Int. Ed.*, 2013, **52**, 11998–12013.
20   C. Y. Huang, in *Methods in Enzymology*, Elsevier, 1982, vol. 87, pp. 509–525.
21   A. Kasprzak and H. Sakurai, *Dalton Trans.*, 2019, **48**, 17147–17152.
22   A. Kasprzak, A. Kowalczyk, A. Jagielska, B. Wagner, A. M. Nowicka and H. Sakurai, *Dalton Trans.*, 2020, **49**, 9965–9971.
23   A. Kasprzak and H. Sakurai, *Chem. Commun.*, 2021, **57**, 343–346.
24   A. Kasprzak, A. Tobolska, H. Sakurai and W. Wróblewski, *Dalton Trans.*, 2022, **51**, 468–472.
25   J. S. Cyniak, Ł. Kocobolska, N. Bojdecka, A. Gajda-Walczak, A. Kowalczyk, B. Wagner, A. M. Nowicka, H. Sakurai and A. Kasprzak, *Dalton Trans.*, 2023, **52**, 3137–3147.
26   H. A. Benesi and J. H. Hildebrand, *J. Am. Chem. Soc.*, 1949, **71**, 2703–2707.
27   S. Goswami, K. Aich, S. Das, A. K. Das, A. Manna and S. Halder, *Analyst*, 2013, **138**, 1903.